Article:
Callaghan, T.V., Romanov, A.N., Khvostov, I.V. et al. (2026) Atmospheric and hydrospheric characteristics in contrasting Arctic and intracontinental regions of Northern Eurasia and possible mutual influences. Water, 18 (2). 251. ISSN: 2073-4441

https://doi.org/10.3390/w18020251

water

MDPI

Article

Atmospheric and Hydrospheric Characteristics in Contrasting Arctic and Intracontinental Regions of Northern Eurasia and Possible Mutual Influences

Terry V. Callaghan [1,2], Andrey N. Romanov [3,*], Ilya V. Khvostov [3], Ivan V. Ryabinin [3], Vasiliy V. Tikhonov [3,4,5] and Olga M. Shaduyko [6,*]

1 School of Biosciences, University of Sheffield, Sheffield S10 2TN, UK; terry_callaghan@btinternet.com
2 Institute of Botany, Tomsk State University (on hold), Tomsk 634050, Russia
3 Institute for Water and Environmental Problems, Siberian Branch, Russian Academy of Science, Barnaul 656038, Russia; nii82@mail.ru (I.V.K.); cgsiena@gmail.com (I.V.R.); vasvlatikh@yandex.ru (V.V.T.)
4 Space Research Institute, Russian Academy of Sciences, Moscow 117997, Russia
5 Arctic and Antarctic Research Institute, Saint Petersburg 199397, Russia
6 Excellence Support Unit, Tomsk State University, Tomsk 634050, Russia
* Correspondence: romanov_alt@mail.ru (A.N.R.); dolcezzamia@mail.ru (O.M.S.)

Abstract

Floods and droughts have increased in Northern Eurasia, probably caused by hydrological changes in other regions. We explore such hypothetical teleconnections by investigating environmental changes in two contrasting harsh environments: the Arctic Kara Sea and the arid Aral–Caspian region. Using long-term data from daily remote microwave sensing, we describe seasonal dynamics of temperature and moisture regimes in the two regions and hypothesize their inter-relationships from new analyses of wind data. For the first time, daily L-band satellite data were used to determine open water in the Kara Sea and long-term seasonal dynamics of brightness temperatures were used to relate variations in the ongoing aridization of the Aral Sea area and abnormal spring floods in the south of Western Siberia. Using soil moisture and Ocean Salinity satellite data, we discovered a previously unrecorded 4-year cyclicity of open-water periods for the Arctic seas and northern parts of the Caspian and Aral Seas. This cyclicity could impact climate forecasting in Northern Eurasia with significant societal implications. The main aim of this paper is to present new analyses that suggest possible mechanisms for teleconnections between the two contrasting harsh environments of Northern Eurasia. The hypothetical teleconnections now need to be tested.

Keywords: Kara Sea; Aral Sea; Aralkum desert; open-water period duration; brightness temperature; satellite SMOS; hypothetical teleconnections

Academic Editor: Adriana Bruggeman

Received: 18 November 2025
Revised: 13 January 2026
Accepted: 14 January 2026
Published: 17 January 2026

1. Introduction

Northern Eurasia is currently experiencing significant climatic and hydrological changes over time that vary in intensity and duration [1]. Possible mechanisms for the observed changes occurring in the northern and southern regions, which belong to different climatic zones, appear to be correlated and may be caused by their mutual influence on each other as an example of climatic teleconnections [2].

According to three observational datasets and 34 climate models, the Arctic has been warming 3–4 times faster than the global average over the past 40 years [3]. As a result,

the total area of perennial sea ice is decreasing, intensive melting of Greenland glaciers continues, earlier melting and later freezing of the tundra occurs, and there is degradation of permafrost and greening and browning of tundra vegetation [4–11]. The south of Northern Eurasia follows this trend with temperature increases of 2 degrees over 92 years and the associated impacts [12]. Such a high rate of warming is due to anthropogenic impacts [11] in combination with natural climate variability [13,14]. The increased rate of warming in the Arctic contributes to a change in the established relationships between the southern and northern regions of Northern Eurasia. Arctic warming reduces the temperature gradient from north to south, which affects atmospheric circulation and, consequently, weather conditions in the northern mid-latitudes. Also, this gradient weakens the polar vortex, which allows colder Arctic air to penetrate further south.

Arctic amplification of warming is expected to increase in the coming decades, which may be associated with further changes in atmospheric circulation [15] and positive feedbacks from the Arctic's surface to the atmosphere, such as increased carbon emissions from thawing permafrost and increased tundra and forest fires, as well as decreases in albedo from reduced areas and seasonality of snow and ice cover [16–19]. Climate and hydrological changes in the Arctic may affect about 5 million inhabitants of the Arctic Circumpolar Permafrost Region [20] and the region's biodiversity [21–24].

The reduction in Arctic Sea ice [24] generates an anomaly of low heat over the Beaufort Sea, causing a Rossby wave in the upper atmosphere. It has been suggested [25] that the summer reduction in sea ice in the Russian Arctic contributes to an increase in forest fires in eastern Siberian high latitudes and the reduction in Beaufort Sea ice cover leads to an increase in the activity of boreal spring fires in Southeast Asia [26]. In turn, forest fires lead to a rapid and irreversible degradation of surface permafrost, the succession of boreal forests, and the subsequent development of potentially dangerous periglacial landforms [27]. Reduced soil moisture and a drier atmosphere after the biomass peak facilitate the availability of more dry fuels [28].

The reduction in total extent of Arctic Sea ice and increased water temperatures that lengthen the open-water periods also enhance evaporation from the Arctic marginal seas [29], leading to a 32% increase in precipitation over land [30] as the loss of sea ice removes a barrier to evaporation, resulting in more humid air masses. The presence of open water also favors upwelling heat currents, warming the troposphere and increasing its capacity to hold water vapor. Increased humidity in Arctic marginal seas during the cold seasons of 1980–2021 (October–March) increased evaporation and thus had a noticeable feedback impact on the extensive further retreat of seasonal sea ice [31].

While atmospheric moisture transport from Arctic Ocean evaporation to Siberia increased significantly during the 1981–2019 fall–winter periods when sea ice began to retreat significantly, Arctic rivers also affect the climate of regions to the south. A change in the hydrological cycle of Arctic river basins [32] alters the atmospheric pressure and wind speeds and directions that transfer cold air masses from northern to southern regions.

In turn, as a result of the atmospheric transport of aerosols from Asia and North Africa, fine mineral dust particles are dispersed over significant distances. These particles influence the Earth's energy balance and trigger climate change on a global scale through interaction with radiation, clouds, and the underlying surface of the Arctic regions. To some extent, they compensate for greenhouse warming in the Arctic [33].

At a regional scale, hydrological changes in the south may affect northern regions including the Arctic [34]. For example, south–north teleconnection effects focusing on the Aral Sea area may include (1) an increase in the frequency of dust storms and atmospheric storms carrying toxic chemicals (mineral salts and pesticide and fertilizer residues) from Aralkum over long distances, including northwards; (2) additional polychemicalization

and the spread of areas of chemical pollution in Northern Eurasia; and (3) atmospheric transport and propagation of heat waves to the north that can cause additional increases in ambient temperatures and a decrease in the duration of the cold period.

We focus here on actual and hypothetical north–south and south–north teleconnections; east–west (and vice versa) teleconnections also occur. The sharp reduction in west-to-east water vapor transport in Central Asia (~15% over the past three decades) is a result of weakening westerly winds; it is also associated with the shallowing of the Aral Sea [34].

Larger scale teleconnections occur, for example, when dust generated by atmospheric storms in Northeast Asia is carried by westerly winds across the globe. This can contribute to global climate change [35]. These dust storms result from changes in atmospheric circulation on a planetary scale. The Arctic Oscillation, which dominates in the middle and high latitudes of the Northern Hemisphere, has a significant impact on the Asian climate. Changes in the Arctic Oscillation are associated with the frequency of dust events in Northern China and the transfer of dust across the Pacific Ocean [36].

It has been reported that high-latitude atmospheric circulation, caused by Arctic warming, increases precipitation in East Asia [37]. A continued warming in the Arctic and further increases in tropical warming are expected to lead to more frequent and intensive heavy rainfall events in East Asia.

Although it is problematic to study the possible interconnected influences of environmental changes and their potential mechanisms in northwestern Siberia and the Aralkum Region, we focused on these two regions because they are extremes—sea ice and deserts—and because these two regions have only a rather sparse network of meteorological or hydrological stations with an accuracy sufficient for practical use. We mainly assess, therefore, possible interconnections that can be inferred from remote monitoring in each territory using satellite data in the visible, infrared, and microwave ranges. This is important because current climate models and climate assessments do not reflect increasing hydrological changes and couplings that can distort climate change predictions and the sensitivity evaluation thereof. In this paper, therefore, we use new analyses of remote sensing data to analyze the long-term seasonal dynamics of brightness temperatures (BTs) (2012–2024) in test areas of the Barents and Kara Seas (in the north) and the Caspian and Aral Seas, large mineral lakes, and the Aralkum Desert (in the south) to hypothesize and predict possible interconnections—teleconnections—affecting hydrological processes of societal importance in these regions. We propose that such hypotheses and predictions be tested in the future to forewarn of environmental changes in both regions that are likely to have severe societal impacts and limit sustainable development goals [38].

2. Materials and Methods

We provide a key to all the acronyms used in the following text (see the Abbreviations section).

The data were obtained from the SMOS satellites (European Space Agency) and analyzed using the software SNAP v.8.0 and SMOS-Box v.5.8.1 (https://step.esa.int/main/download/snap-download/). Linear regressions were calculated by autoregressive integrated moving average (ARIMA) model. Graphs and figures were drawn with Microcal Origin v.6.0.

2.1. The Two Study Areas and Their Changing Environments

The macroregions under study are Western Siberia and part of Central Asia, stretching from the Kara Sea in the north to the Aral Sea in the south. This territory is characterized by significant differences in nature and climatic conditions and includes the following main natural zones: marginal seas, tundra, forest tundra, taiga, forest steppe, steppe, semi-desert,

and desert (Figure 1). However, we focus on the two extremes, i.e., the Kara Sea and the Aral Sea regions.

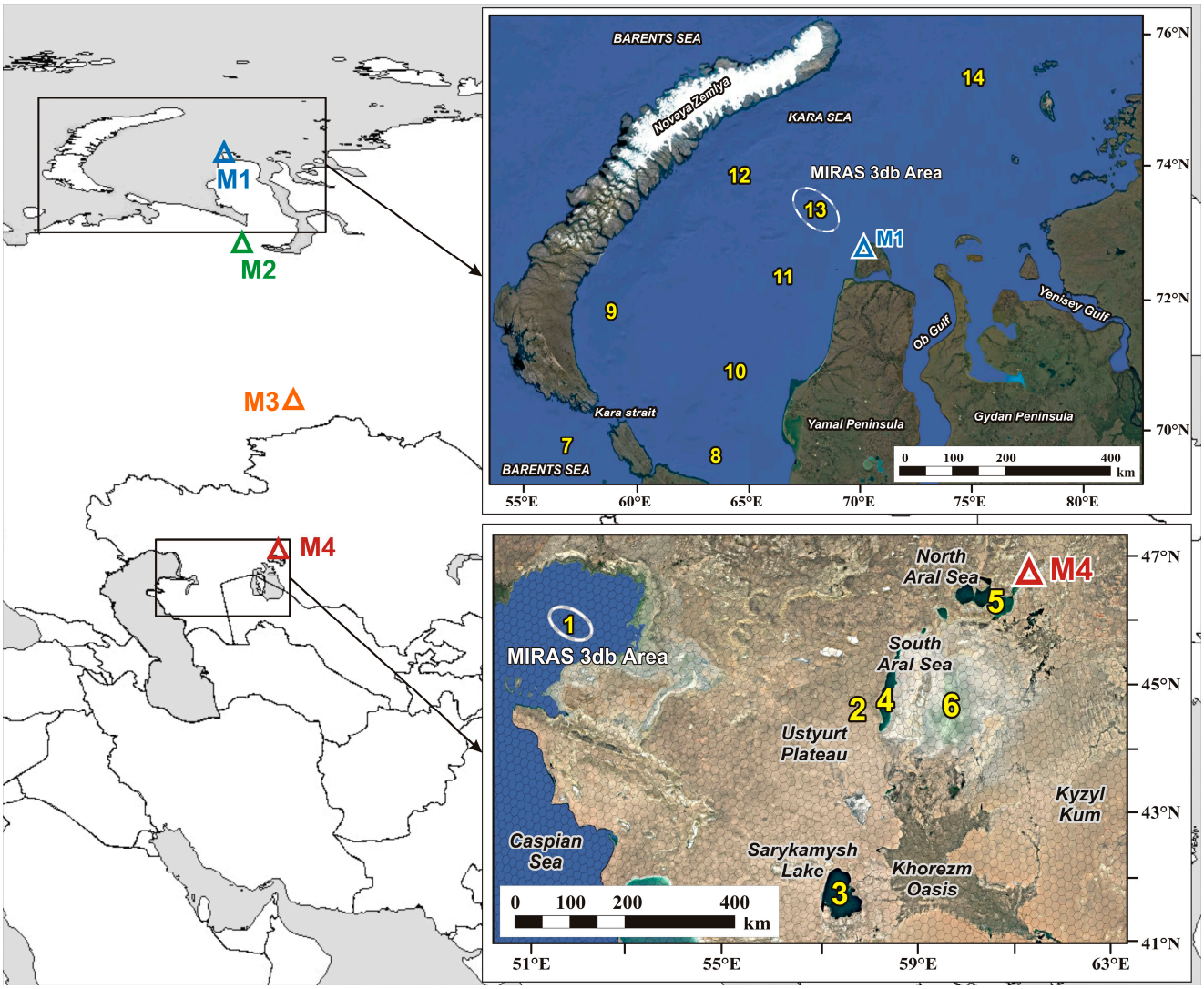

Figure 1. Maps of test areas (1–14) and meteorological stations (M1–M4).

Optical methods are unable to detect the seasonal dynamics of hydrological and climate changes due to frequent cloud cover and shallow sounding depth (microns). In contrast, the use of daily satellite microwave data allows us to study the areal characteristics of the underlying surface in a certain effective emitting layer, the thickness of which is determined by the wavelength of a satellite radiometer and, unlike optical methods, can vary from a few millimeters (for the water surface) to several meters (for ice cover) [39]. Analysis of daily BT data, independent of cloud cover, enables us to study the seasonal dynamics of hydrological parameters, such as the duration of open-water, ice cover (for seas and large lakes with seasonal ice cover), and seasonal soil freezing periods [40], characterizing climatic changes in the region.

The scientific literature lacks for a detailed analysis of teleconnections based exactly on diurnal remote microwave sensing data since reliable daily SMOS information began to arrive only in December 2012, and time series data have not been accumulated yet. Statistical analysis of the time series of meteorological parameters was therefore clearly beyond the scope of this work. However, we explore possible statistically significant

relationships to describe the open-water periods in the Kara and Caspian Seas, as well as in the northern part of the Aral Sea.

The choice of these two regions with very different physical characteristics and located in the north and south of Northern Eurasia was motivated by the presence of large water bodies (seas and lakes) with seasonally formed ice cover. The duration of open-water and freeze-up periods serve here as the main climate-dependent parameters. Consequently, it becomes possible to compare the hydrological and climatic characteristics of these regions based on the fundamental differences in brightness temperatures (BTs) of the water surface and ice cover in the microwave frequency range. These values are easily determined due to the year-round daily measurements of BTs from the SMOS satellite (European Space Agency) (which orbits the Earth in 104 min) ranging from twice (at the equator) to thirteen times (at the poles) per day, depending on the geographic latitude of the location. Year-round observations allow us to study the seasonal dynamics of open-water and freeze-up periods. Long-term seasonal dynamics of open-water periods contribute to assessing trends in hydrological and climatic changes.

2.1.1. The Kara Sea Study Area

We study the area of the Kara Sea between Novaya Zemlya and the Yamal Peninsula, including the eastern part of the Barents Sea that is influenced by the warm Gulf Stream.

The long-term seasonal dynamics of the radio brightness temperatures of the water surface of the water bodies with a seasonal ice layer that we study depends on the combined influence of the thermodynamic temperature and salinity of the water, as well as the temperature, salinity, thickness, and concentration of the ice. From October to June, the Kara Sea is covered by first-year ice of local origin. Ice thickness varies spatially within 0.5–1.5 m. In winter, at the boundary with air, the ice temperature drops below −45 °C, whereas the under-ice water temperature is close to the freezing point (−1.8 °C). In summer, the sea surface warms up from 2 °C (in the north) to 6 °C (in the south). Salinity (S) varies from 3–5% in the south to 33–34% in the north. A decrease in S in seawater occurs due to river runoff, and ice and snow melting. The spatial distribution of desalinated water varies annually and can vary even during one summer [41].

Analysis of SMOS (Soil Moisture and Ocean Salinity) data shows that, in all areas of the Kara Sea, the duration of the open-water period increases in summer periods, and that is accompanied by a proportional reduction in the duration of the freeze-up period in winter [42]. The rate of sea ice loss in the Arctic Ocean, including the Kara Sea, in the summer period is accelerating [43], primarily due to rising air temperatures [44]. Ice cover during the winter period has also significantly decreased [45], and the ratio of different forms of ice has also changed [46].

All these changes have been observed against the backdrop of a decrease in the severity of winter conditions for the study area (from the 1980s up to 2022) [47].

2.1.2. The Caspian–Aral Region and Aralkum Desert Study Area

In the arid regions of Central Asia, monitoring desertification processes intensified in the 1960s as a result of the catastrophic drying up of the Aral Sea and continue to this day [48,49]. The main causes of desertification are the overall decrease and seasonal redistribution of precipitation in the region [50], an increase in the temperature of the underlying surface, an increase in the duration of dry periods, and soil salinization as a result of wind transfer of toxic salts [51–53]. The drying up of the Aral Sea was also caused by the expansion and poor management of irrigation in the upstream areas of the Syr Darya and Amu Darya [54]. The long-term impact of all of these negative factors on the

environment can lead to significant changes in the water balance of wider areas of Central Asia and the hydrological cycle [55].

The area of the Aral Sea decreased from 68,000 km^2 in the 1960s [54] to 5130 km^2 in 2025 [56] (https://www.cawater-info.net/aral/data/monitoring_amu_e.htm accessed on 10 September 2025)—more than 13 times. The change in the area of the Aral Sea during 2000–2015 was determined using MODIS (Moderate Resolution Imaging Spectroradiometer) satellite images, and the sea level was determined using altimeters installed on the Topex/Poseidon, Jason-1, Jason-2, Envisat, and SARAL (Satellite with ARgos and ALtiKa) satellites [57–59]. Long-term monitoring continues by the Interstate Commission for Water Coordination of Central Asia using Landsat 8 satellite images and field monitoring and processing.

As a result of many years of drying out, the Aral Sea broke up into two separate basins: the North Aral Sea (NAS) and the South Aral Sea (SAS). The latter subsequently broke up into the West basin (WB) and East basin (EB) of the SAS.

As a result of particularly strong drying out in 2009 and 2014, the EB of the SAS almost completely dried up within a few months, leaving behind an exposed bed. This led to more frequent dust storms, and the formation of large amounts of salty dust, which poses a serious threat to the environment and human health [60–63], vegetation degradation and, as a result, further desertification of territories and a significant deterioration of the environmental situation, not only in Central Asia but also in neighboring regions. The Aralkum sand–salt desert was formed in place of the exposed bottom of the EB of the SAS [64–67]. The drying out of the Aral Sea was accompanied by an increase in water salinity [68]. Spatio-temporal changes in vegetation and soil cover characteristics were tracked in the vicinity of the former Aral Sea between 2003 and 2018 using Landsat and MODIS Aqua data [69–71].

2.2. General Approach

As mentioned earlier, it is problematic to study the possible interconnected influences of environmental changes and their potential mechanisms in northwestern Siberia and the Aralkum Region using a rather sparse network of meteorological or hydrological stations with an accuracy sufficient for practical use. However, assessing possible interconnected influences can be inferred based on remote monitoring of each territory using satellite data in the visible, infrared, and microwave ranges.

When predicting climate change in the Arctic (northern study area), an important factor is the ratio of the duration of open water and continuous ice cover periods, since changes in the thickness and area of the ice cover have a strong effect on heat flows between the ocean and the atmosphere. Microwave radiation from the marginal seas of the Arctic Ocean undergoes sharp seasonal changes associated with the formation and melting of ice cover on the water surface. During the period of ice freezing, changes in the brightness temperature (BT) of the sea surface depend on the temperature and salinity of sea ice and its thickness and concentration, including the temperature and density of the snow cover. The emissivity of the sea depends on the properties of the multilayer system "water + ice + snow + atmosphere" [72,73]. Contrasts in the BTs of thin sea ice can exceed 25 K depending on ice thickness, salinity and temperature, and the thickness and wetness of the overlying snow [74]. Satellite data in microwave, infrared, and optical ranges are used to identify ice cover and water surfaces [75].

Relevant to the southern study area, data from the MODIS device installed on the Terra and Aqua satellites are widely used to monitor surface temperature [76,77]. For example, the integral moisture content of the atmosphere may be reconstructed using data from the SSMIS (Special Sensor Microwave Imager/Sounder) microwave radiometer installed

on the DMSP (Defense Meteorological Satellite Program) satellites [78]. To determine soil moisture and sea water salinity for the northern study area, data from the SMOS and SMAP (Soil Moisture Active Passive) satellites may be used [79–81]. A comprehensive analysis of remote and ground-based studies allows us to identify ongoing hydrological and climatic changes, as well as to study the mechanisms of mutual influence of different regions on each other [82].

Operational data on the hydrological response to climate change can be obtained using microwave remote sensing methods [83]. Satellite data at a frequency of 37 GHz are used to determine the onset of the melting and freezing of sea ice [84]. Remote sensing data have proven a decrease in the volume and area of sea ice in the Laptev Sea in 1979–2002 [85]. In addition, these data were used to estimate the minimum extent of sea ice in the Beaufort, Laptev, Chukchi, East Siberian, Kara, and Barents Seas [86]. Satellite measurements were also used to estimate the concentration and area of sea ice in the polar regions [87]. Remote microwave monitoring of the water surface is based on the dependence of water emissivity on temperature (T) and salinity (S) [88–92]. Remote measurements of T and S in the surface layer of the World Ocean are used to assess global climate changes occurring in the ocean–atmosphere system [93]. To improve the accuracy of remote sensing of S measured at different angles of incidence [94], spatial data on S are compared with precise contact measurements from buoys [95], as well as with a priori data on the ocean surface [96–99]. Microwave, infrared, and optical ranges are used as satellite data [100].

Long-term seasonal dynamics of the radiative characteristics of the underlying surface carries information about seasonal changes in the spatio-temporal distribution of temperature and moisture of the soil cover, temperature, and salinity of the World Ocean and inland water bodies, and the duration of warm and cold periods. In turn, information about ongoing hydrological changes allows us to move on to qualitative and quantitative characteristics describing dangerous meteorological and hydrological phenomena (the severity of winter, abnormally cold and abnormally hot weather, extreme heat, severe frost, winter thaw, summer frosts, waterlogging of the soil, drought, etc.).

2.3. Data Sources and SMOS Satellite Data Analysis Algorithm

To assess hydrological changes in Northern Eurasia, we used daily data from the SMOS satellite measured in the microwave range and calibrated in units of brightness temperatures. In addition, known patterns of microwave radiation for soils, water surfaces, and ice cover were used with variations in their physical characteristics (soil moisture and temperature, water temperature and salinity, and ice cover temperature and concentration) [79].

The intensity of microwave radiation can be expressed through the brightness temperature T_B (B—brightness), according to the formula [101]

$$T_B = \chi T_{ef},$$

where χ is the emissivity of the underlying surface, T_{ef} is the effective temperature of the material medium in the thickness of the microwave emission-forming layer (skin layer) L_{ef}, defined as a value inversely proportional to the absorption coefficient γ [101].

$$L_{ef} = \frac{\lambda}{4\pi\sqrt{|\varepsilon|}tg\delta} = \frac{1}{2k_0\kappa} = \frac{\lambda}{4\pi\kappa} = \frac{1}{\gamma},$$

where k_0 is the wave number in free space, κ is the absorption index, ε is the complex dielectric permittivity of the medium, and $tg\delta$ is the dielectric loss tangent.

The quantities T_B and χ are the main characteristics describing the radio-emitting properties of the underlying surface. The effective temperature of a half-space having a temperature gradient in the direction of the z-axis when receiving its own thermal radiation propagating along this axis can be calculated using the following formula [101]:

$$T_{ef} = T_0 + \int_0^\infty \frac{dT}{dz} e^{-\int_0^\infty \gamma(z\prime)dz\prime} dz,$$

where T_0 is the surface temperature, dT/dz is the local temperature gradient, and $\gamma(z)$ is the absorption coefficient in the skin layer L_{ef}, determined by the formula [101]

$$\gamma(z) = \frac{4\pi}{\lambda} \sqrt{\frac{\varepsilon' - sin^2\theta}{2} \left[\sqrt{1 + \left(\frac{\varepsilon''}{\varepsilon' - sin^2\theta} \right)^2} - 1 \right]},$$

where ε', ε'' is the real and image part of the complex dielectric permittivity.

If there is no temperature gradient, then $T_{ef} = T_0$.

The given relationships establish a correlation between the T_B values measured by the SMOS satellite and the dielectric characteristics of natural media samples (water, ice, and soil) defined in laboratory conditions. Calibration and validation of satellite data are carried out based on a comparison of satellite and laboratory data (see, for example, [102,103]).

2.4. Remote Sensing Data

To analyze hydrological changes, we use SMOS data calibrated in brightness temperature units. The MIRAS (Microwave Imaging Radiometer with Aperture Synthesis) 2D interferometer installed on the satellite receives upwelling radiation at a frequency of 1.41 GHz. The maximum dependence of the radiometer bandwidth on the incidence angle is at θ = 42.5°; the transverse spatial resolution is 35 km; and the longitudinal resolution is 65 km [104]. SMOS (L1C product) contains horizontal (T_{BH}) and vertical (T_{BV}) polarizations measured in the range θ = 0–60° [105]. The L1C data are presented in the form of a discrete geodetic grid (DGG) ISEA 4H9. The linear cell size is 16 km; the area is approximately 195 km^2 [106].

In this study, we use T_{BH} (from L1C), corresponding to θ = 42.5°. To ensure maximum reliability, the following source data are excluded from the analysis: (1) those burdened by the influence of radio frequency interference (according to the RFI1 quality feature); (2) those obtained outside the Alias Free region of overlapping replicas (AF quality feature); (3) those with an error of ΔT_{BH} greater than 5 K; and (4) those with polarization coefficient values (T_{BH}/T_{BV}), lying outside the range from 0.01 to 0.99. The spatial distribution of T_{BH} is compared with MODIS satellite images obtained for the same territory.

Emissivity coefficients of the open-water surface and the formed ice cover differ by a factor of three, thus corresponding to a difference in BT values of at least 160 K. Therefore, for binary differentiation of the water surface state, the accuracy of SMOS data on BT (3–15 K) is clearly adequate. The proximity of land to the study grid cell has an effect on the corresponding BT value. Emissivity of the water area in this wavelength range is determined mainly by the temperature and mineralization of the water and waves, and the state of the ice cover. Emissivity of land depends on temperature, humidity, mineralization, availability, and the phenological basis of vegetation. However, in the absence of active interference sources, the presence of a radio brightness contrast sufficient for differentiating the state of the water surface is preserved even with an equal ratio of water and land areas forming the radiation attributed to the cell [107]. Moreover, the greater the contribution of lands adjacent to a water body, the higher the accuracy requirements for BT values (the ΔT_B criterion). The T_{BH}/T_{BV} criterion is designed to exclude situations with strong waves and

overestimation of T_{BH} values relative to calm water conditions. The RFI criterion is derived to exclude situations with the influence of active interference sources. Typically, we use solely T_{BH} values, as they are less sensitive to the type and height of potential vegetation in adjacent land areas.

The criteria were obtained empirically in the course of developing the algorithm for determination of the boundaries of phenological phases in the Kara Sea through the use of a dataset of 60 cells (2012–2015) [108]. The criteria were then refined by applying the datasets of 30 cells for the Aral–Caspian region for the same period. Weakening the criterion for ΔT_B results in poor determination of the boundaries of phenological phases (false positives in the algorithm), while strengthening the requirements for ΔT_B causes excessive thinning of the time series and, consequently, decreasing accuracy in defining the boundaries of phenological phases.

The cells of the DGG ISEA 4H9, which fall within the pixels of the SMOS satellite, were selected as the main test areas in the Barents Sea (7—id4046992) and in the Kara Sea (8—id4052100, 9—id4055708, 10—id4056717, 11—id4063891, 12—id4068512, 13—id4069015, and 14—id4082841) (Figure 2).

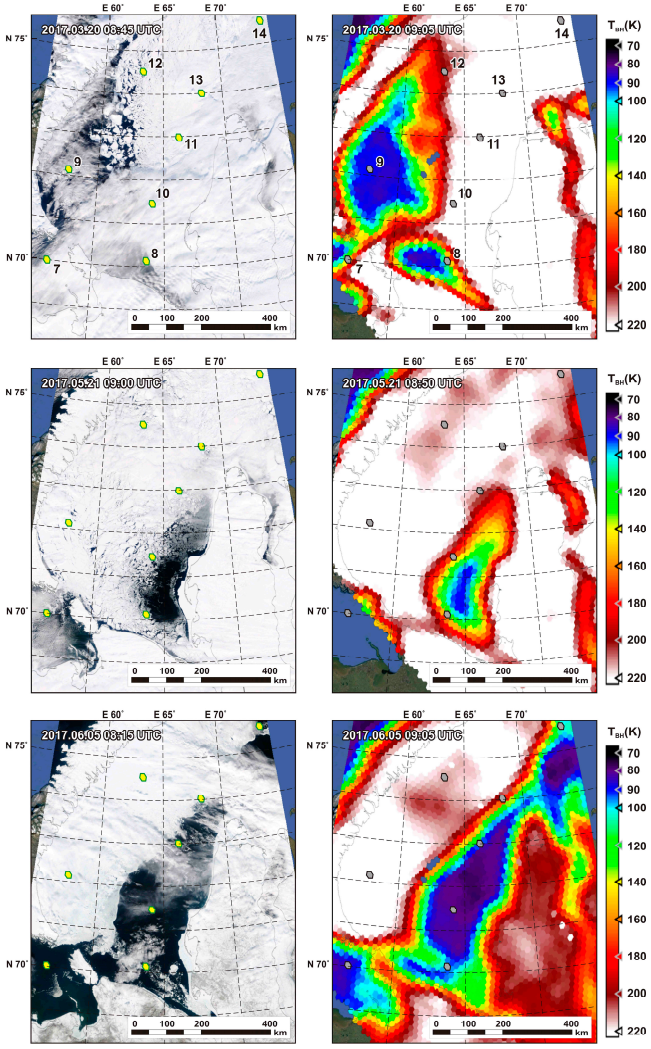

Figure 2. MODIS optical images of the Kara Sea and spatial distribution of BT (L1C SMOS product) in different periods of 2017; marked points (ISEA cells): 7—id4046992 (Barents Sea), 8—id4052100, 9—id4055708, 10—id4056717, 11—id4063891, 12—id4068512, 13—id4069015, and 14—id4082841. The vertical axis on the left is degrees north, while the right axis is brightness temperature. The color hexagons on the right side are T_{BH} (K) with the key on the right side of the figure.

Figure 2 makes it possible to evaluate the correspondence of nearly simultaneous optical and microwave satellite images. It shows the presence of huge areas of open water in 2017 already in late March (not in May or June, as usual). This is clearly visible in both ranges. Ice-covered areas of the water area are almost indistinguishable in MODIS images from cloud-covered sites.

We use infrared MODIS data (surface temperature values) only from cloud-free areas. The surface emissivity is determined by the ratio of the brightness temperature (SMOS) to the thermodynamic temperature (MODIS). For estimating the spatially averaged emissivity of a homogeneous surface, pairs of nearly simultaneous infrared (MODIS) and microwave (SMOS) satellite data are used.

Table 1 contains the numbers of cells of the discrete geographic grid used in some products (satellite data sets) from the European Space Agency [106]. The coordinates of points (centers of the grid cells) are given in Table 1. The dates and times of the images are shown in Figure 2.

Table 1. Numbers of DGG cells for seas (Figure 1).

№	DGG ID [105]	LAT	LON
1	3077728	45.978	51.383
2	3097187	44.857	57.843
3	3094604	41.957	57.404
4	3098724	44.857	58.326
5	3107445	46.307	60.985
6	3103335	44.813	59.799
7	4046992	69.948	56.819
8	4052100	70.165	63.756
9	4055708	72.158	57.790
10	4056717	71.486	64.117
11	4063891	72.990	66.232
12	4068512	74.523	63.347
13	4069015	74.025	67.800
14	4082841	75.963	77.960

Figure 3 presents the seasonal dynamics of $T_{\mathrm{BH}}(JD)$ of two test sites in the Barents and Kara Seas. The abscissa axis shows the values of the Julian day JD_{2012} counted from the beginning of the observation period (1 January 2012). Markers $JD_1 - JD_4$ highlight the dates of the beginning of qualitative changes in emissivity of the water area. Below, based on the analysis of time series from SMOS, the phases of the ice regime are determined.

2.5. Algorithm for Determining Ice Cover Periods Using SMOS Satellite Data

The open-water period (OWP) is the time interval between JD_1 and JD_2 characteristic of ambient temperature (T_{A}) exceeding that of ice formation from saltwater (T_{SW}). Values T_{BH} = 82 $\pm$ 12 K depend on water temperature and salinity, the intensity of sea waves, and the resultant foam [109]. The increase in T_{BH} may be caused by drifting ice and the desalination of sea water induced by ice melting.

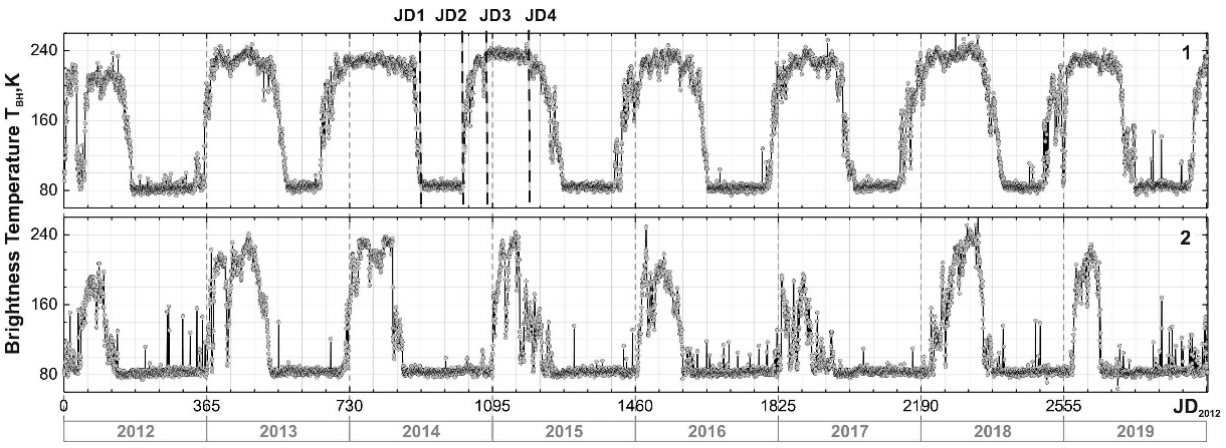

Figure 3. Seasonal dynamics of brightness temperature for the points in the Kara (1) and Barents (2) Seas.

To determine OWP, we propose the following algorithm. A surface is assumed to be free from ice if within 3 days T_{BH} does not exceed its arithmetic mean for the period from July 15 to October 15 of a given year. The half-width of the range is identified by the statistical spread in values for this period increasing by the greatest possible determination error ΔT_{BH} = 5 K, not exceeding ΔT_{BH} = 12 K. The beginning of the period is considered to be the date after which values of T_{BH} can differ only within 10% from those typical for this period for at least 3 days. The end of this period is the date from which T_{BH} can differ by more than 10% for 3 or more days.

The 10% threshold was obtained statistically when developing the algorithm for determining the boundaries of phenological phases of the Kara Sea by using a dataset for 60 cells (2012–2015) [108]. In the case of the algorithm's application to other water areas and periods, this value did not change.

Data binding to the average T_{BH} value for a period with ice-free water made the algorithm consistent across all grid cells of the Arctic Ocean, regardless of the degree of mineralization. For waters of the Aral–Caspian region, the average for the first and fourth quarters of this period was used.

Initially, the algorithm used 30-day values to detect changes in the phenological phases of the Kara Sea. A period reduction to 3 days allowed us to record short ICFP periods in waters at more southern latitudes and to detect multiple phase changes (noise) at the end of the OWP (in this case, a group of consecutive ICFP phases merged into one). Reduction to less than 3 days resulted in false positives in the algorithm. The parameter was selected empirically.

The algorithm was tested on a grid cell dataset for waters of the Laptev and Baltic (Gulf of Bothnia) seas from 2012 to 2015 [110] and the Barents and Kara seas in 2012–2024. The results are consistent with the satellite optical data.

The period of ice cover formation (ICFP) is the time interval between JD_2 and JD_3 when ice cover (with a skin layer thickness of d, $d \geq L$, L) is formed on the water surface shielding the emissivity of the latter. During this period, T_{BH} varies between 90 and 220 K. Its variations are related with the increase in d and the occurrence of interference phenomena due to changes in the λ/d ratio. From the analysis of dependences $T_{BH}(JD)$ in Figure 3, it follows that a transition from open water to continuous ice cover formation in different parts of the Kara Sea takes place within 20–40 days. Variations in T_{BH} reach 150 K. This is due to the fact that in winter the ice cover can be partially or completely destroyed by storms and strong winds, especially during the formation of transitional forms of sea ice (nilas) at low d values.

The period of complete ice cover (CICP) is the time interval between JD_3 and JD_4. Based on dependences T_{BH}, it is typical for $T_A < T_{SW}$ at $d > L$ ice cover thickness on the water surface. Values of T_{BH} vary from 210 to 230 K and probably depend on T and S of ice, ice cover cohesion, and snowfield presence on its surface during thaws.

Attention is drawn to ΔT_{BH} = 30–50 K, which can be caused by (1) abnormally low temperatures ($T < -45$ °C), at which the salt solution in the micropores of sea ice freezes, dielectric losses significantly decrease, and ice cover no longer shields microwave radiation of the water lying beneath it ($L > d$); (2) extended sections of open water appear in cases when the continuous ice cover is destroyed. The combination of microwave measurements with satellite data in the visible (ice concentration) and infrared (surface temperature) ranges makes it possible to separate these effects. The duration of CICP, determined by the number of days between JD_3 and JD_4, characterizes hydrological changes occurring in the Arctic. Temporal trends in the duration of the cold period indicate the direction of climate change.

The period of ice cover destruction (ICDP) is the time interval between JD_4 and JD_1; it is transitional from negative to positive temperatures. Values of T_{BH} are within 210–230 and 90–85 K. Variations in T_{BH} are probably caused by the melting of snow on the ice surface. If the annual sea ice is thin, the appearance of microcracks (through which water rises) at the ice–water boundary is among the reasons for T_{BH} reduction. This effect brings decreases in the brightness temperature until the water in the ice microcracks freezes again [111]. Short-term variations in T_{BH} in spring can be associated with the formation of multilayered ice cover and the appearance of water layers there as a result of the surface ice melting and the subsequent freezing of the meltwater [112].

3. Results

3.1. Kara Sea and Yamal Tundra

Prior to using microwave satellite data to estimate the seasonal dynamics of brightness temperatures, it was necessary to validate the reliability of these data. To achieve this, SMOS satellite data were compared with MODIS infrared radiometer data (MODIS data were used only to demonstrate the qualitative agreement between optical and microwave data; joint processing with SMOS data was not performed). Figure 2 shows the spatial distribution of T_{BH} for the Kara Sea and the eastern Barents Sea in different seasons (on the right). For comparison (on the left), MODIS satellite images for the same (or close) dates are shown. It is evident that the brightness temperatures of different parts of the sea differ significantly. The values of $T_{BH} < 90$ K correspond to open-water areas, which is confirmed by comparison with MODIS data (https://worldview.earthdata.nasa.gov accessed on 25 December 2025). The T_{BH} value varies from T_{BH}^{W} (water surface) to T_{BH}^{I}. (solid ice cover). When comparing the spatial distribution fields with the corresponding time optical images, the studied part of the Kara Sea turns out to be ice-free from 15 July to 15 October every year (2012–2021).

From the results of the analysis of SMOS and MODIS data, it follows that the open water areas determined by MODIS data coincide with the water areas determined by SMOS data. However, at the same time, areas identified as water by SMOS data may be identified as ice cover by MODIS data. From comparison of the figures, it is clear that the areas of the sea with low values of radio brightness temperature (according to SMOS data) correspond to areas of the sea that are free of ice cover (according to MODIS data). Figure 4 shows OWP trends indicating cyclic changes in the Arctic approximated by the formula

$$N = A + B \times cos\left(2\pi \frac{x - x_0}{w}\right) \quad (1)$$

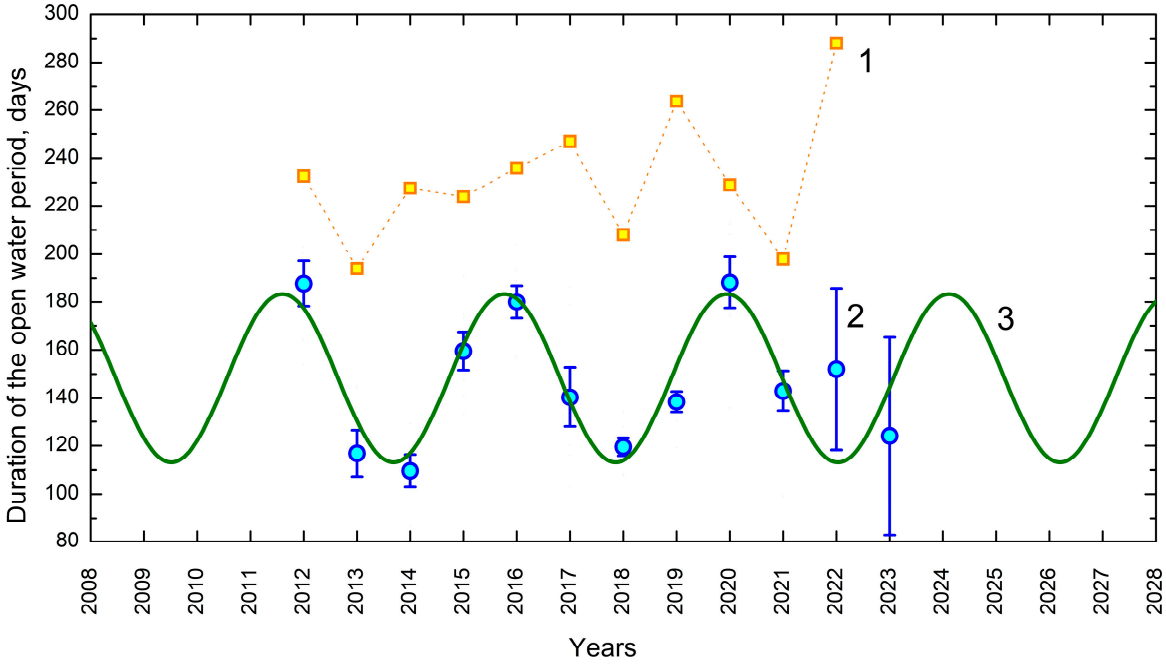

Figure 4. Predicted duration of the open-water period for test area 7 in the Barents Sea (marked 1, yellow squares with dashed line), averaged for test areas 8–14 in the Kara Sea (marked 2, blue circles), and appoximation by a harmonic function (Formula (1)) for the Kara Sea average values (marked 3, green line).

Numerical coefficients are given in Table 2.

Table 2. Comparative analysis of statistical characteristics (Formula (1)) for different seas.

Object	A	B	x_0	w	R^2	χ^2
Kara Sea	144.6	36.4	2012	4	0.83	160
North part of Aral Sear	240.7	11.75	2012	4	0.71	32
North part of Caspian Sea	285.0	28.75	2012	4	0.82	103

Note: χ^2 is the chi-squared test.

In 2012–2023, maximum amplitudes of N varied between 113 and 183 days. It follows from Formula (1) that the predicted duration of OWP until 2028 for the Kara Sea is on average 148 days without regard for anthropogenic factors and climatic changes in the Arctic. The significant data scattering in 2022 and 2023 was due to increased interference.

From Figure 4 it follows that, for the Kara Sea area, there is a 4-year cyclicity of open-water periods. The same figure shows a graph of the dependence approximated by sinusoidal Formula (1).

The nature of this cycle has not been studied in detail. It has been suggested that a similar decaying cycle (manifested in 2012) could have been caused by an atmospheric-hydrospheric process responsible for the occurrence of severe drought (2012), which affected many regions of the world, including North America and Eurasia. In turn, 2012 saw the lowest number of north–south winds recorded at the meteorological station (Bely Island) in the 1965–2025 time range, which could increase the intensity and scale of the drought. Determined from SMOS data, annual variations in the duration of open-water periods reached 80 days. In 2016, abnormally hot weather occurred in Western Siberia [113–115]. In 2020, this region also suffered from severe drought (Omsk and Novosibirsk Oblasts, and Altai Krai) [116] with total damage exceeding one billion rubles.

In 2014 and 2018, anomalous catastrophic spring floods occurred here (Altai Krai and Tuva) causing significant damage to the region's infrastructure and resulting in human casualties. Figure 4 demonstrates minimal values of OWP during these years. This suggests that extremely high temperatures in Central Asia and Western Siberia at the beginning of summer may contribute to OWP prolongation. In turn, abnormal spring floods contribute to the cooling of the underlying surface, thus preventing the emergence of heat waves.

3.2. Caspian–Aral Region

Figure 5(1)–(5) show the long-term seasonal dynamics of $T_{\mathrm{BH}}(JD)$ of the underlying surface (the Earth's surface) from 2012 to 2024. The $T_{\mathrm{BH}}(JD)$ for the northern part of the Caspian Sea is typical for water bodies with seasonal ice cover formed on the water surface (Figure 5(1)) (similar to Figure 3(1)).

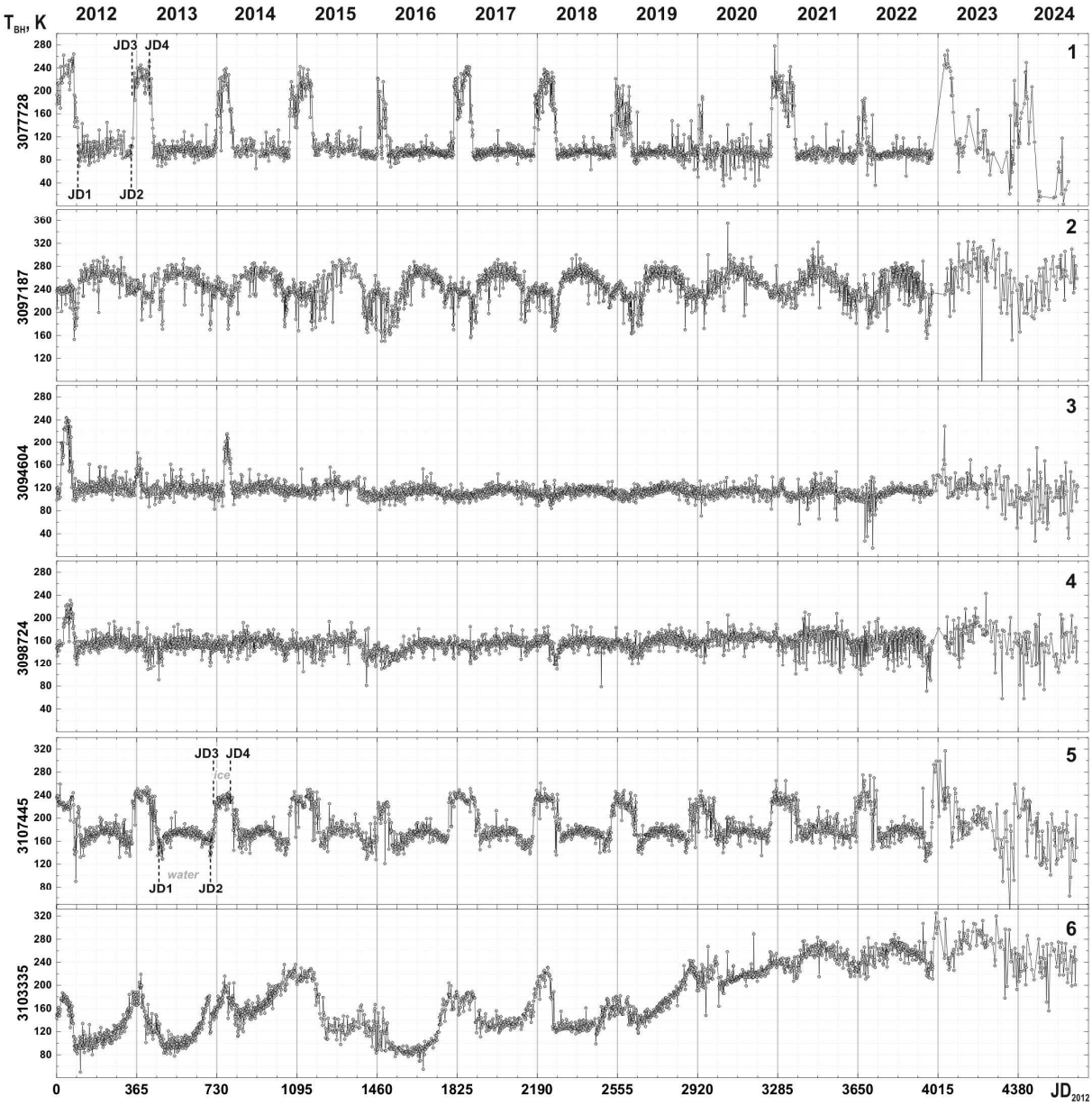

Figure 5. Long-term seasonal dynamics of $T_{\mathrm{BH}}(JD)$ on horizontal polarizations: 1—northern part of the Caspian Sea; 2—steppe between the Caspian and Aral Seas; 3—hypersaline lake Sarykamysh; 4—the WB of the SAS; 5—NAS; 6—salt marsh formed as a result of the drying out on the former basin of the Aral Sea.

The seasonal dynamics of $T_{BH}(JD)$ for the steppe area located between the Caspian Sea and Aral Sea are typical of seasonally frozen soils (SFSs) (Figure 5(2)). In the warm period, the radio brightness contrasts $\Delta T_{BH} \approx 30$ K are associated with the influence of temperature and soil moisture; in the cold period, $\Delta T_{BH} \approx 60$ K is associated with seasonal soil freezing. A specific feature of SFS microwave radiation is the existence of four periods with different soil cover radio emissivity characteristics: 1—unfrozen soil (JD_1–JD_2); 2—SFS with a seasonally frozen layer of thickness $d \leq L$ (L is the SFS skin layer) (JD_2–JD_3); 3—SFS with $d \geq L$ (JD_3–JD_4); and 4—SFS thawing (JD_4–JD_1).

Figure 5(5) shows $T_{BH}(JD)$ for NAS. ΔT_{BH} values reaching 150 K are associated with phenological features of ice cover formation on the water surface. Trends in duration of OWP, calculated on the basis of $T_{BH}(JD)$ analysis and being radio-physical indicators of hydrological and climatic changes, indicate that duration of OWP variations amount to 250 ± 15 days.

At the same time, from the long-term seasonal dynamics of $T_{BH}(JD)$, shown in Figure 5(3) (Sarykamysh Lake) and Figure 5(4) (WB of SAS), noticeable differences from NAS and the Caspian Sea are visible. Ice cover was formed on Sarykamysh Lake in 2012–2014 (Figure 5(3)), and on the West Basin of the Southern Aral Sea (WB of SAS) in early 2012 (Figure 5(4)). In subsequent years, the surfaces of these water bodies were free of ice all year round. The observed variations $\Delta T_{BH}(JD) \approx 10$–$15$ K are associated with seasonal changes in water temperature and, probably, salinity. From the analysis of seasonally freezing and year-round non-freezing water bodies located in the same region with the same climatic conditions, it can be assumed that those hydrological changes in the WB of the SAS and Sarykamys can be caused by an increase in the concentrations of mineral salts and organic substances dissolved in the water, which result in a decrease in the freezing temperature of the water. The area and salinity of Sarykamys Lake are currently unstable and depend on the volume of collector drainage water entering the lake and the concentration of mineral salts and chemicals in them. For example, in 1985, the area of the lake's water surface was 3200 km^2, and salinity was 15–20‰.

Figure 5(6) shows the long-term seasonal dynamics of $T_{BH}(JD)$ for the dried-up EB of the SAS, which is currently the sandy, salty desert of Aralkum. In 2012–2013, $T_{BH}(JD)$ had an appearance typical of a water surface with seasonal ice cover. Starting from March 2013 to May 2015, the gradual increase in variations was insignificant and amounted to 250 ± 15 days. T_{BH} values from 90 K to 260 K were observed. Such behavior of $T_{BH}(JD)$ can be associated with the drying up of the inland sea, and probably an increase in the salinity of the remaining water. However, from mid-2015 to 2018, the behavior of $T_{BH}(JD)$ changes again and becomes similar to the $T_{BH}(JD)$ of a water surface with seasonal ice cover. Such a significant change in $T_{BH}(JD)$ was caused by the discharge of water from NAS to the EB of the SAS, through the culverts at the Kokaral dam. From 2018 to the present, T_{BH} variations are $40 \div 80$ K, and may be associated with changes in ambient temperature and the redistribution of precipitation, which contribute to an increase or decrease in the moisture of the underlying sandy salt marsh surface of Aralkum.

Changes in the seasonal dynamics of $T_{BH}(JD)$ indicate ongoing aridization of the territory, which is manifested in an increase in T_{BH}.

Figure 6 shows the long-term dynamics of open-water period (OWP) days for the northern part of Aral Sea and the northern part of Caspian Sea, determined using SMOS satellite data. It is evident that a four-year OWP cycle is observed in all graphs for the Kara Sea, Caspian Sea, and Aral Sea. This similar behavior in long-term OWP dynamics indicates the existence of a global (macroregional) process, a mechanism influencing Northern Eurasia with a four-year period. Figure 6 presents OWP trends indicating cyclic changes in

the northern parts of Caspian and Aral seas approximated by Formula (1). The numerical coefficients are given in Table 2.

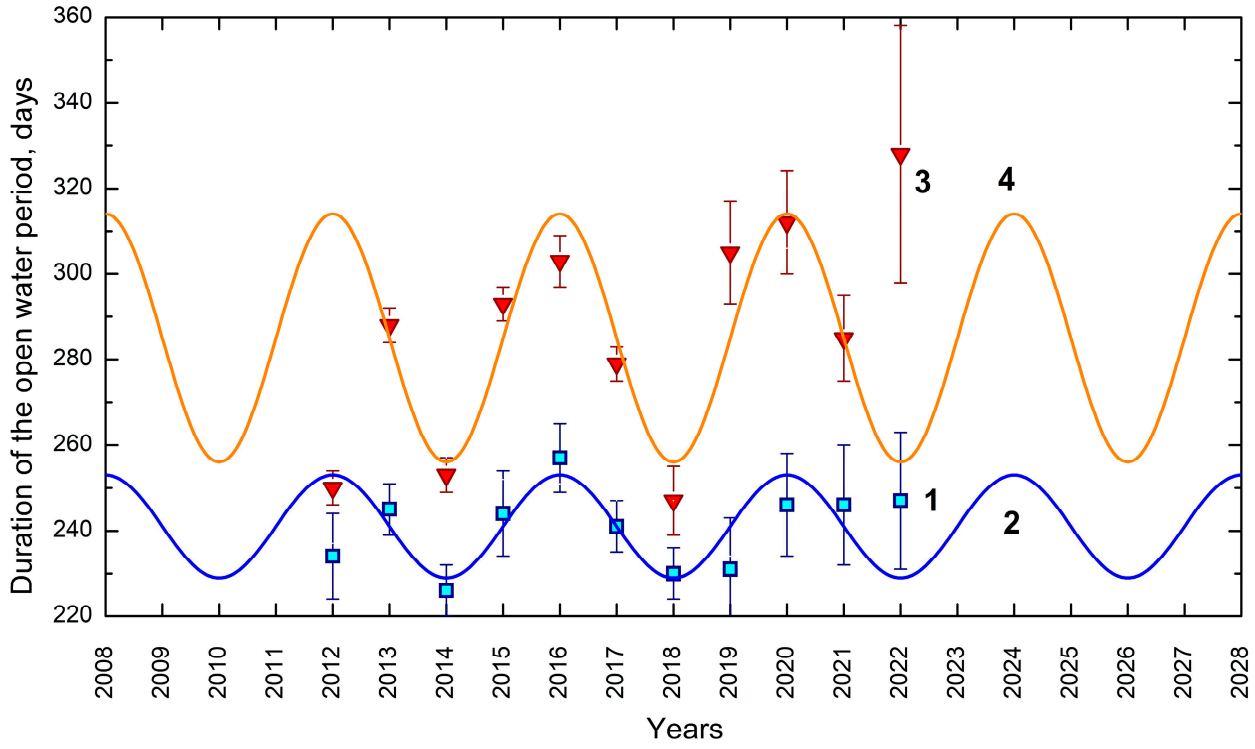

Figure 6. Observed duration of the open-water period days for the northern part of Aral Sea (1, blue squares), the northern part of the Caspian Sea (3, red triangles). Modeled data from Formula (1) dependences for the northern parts of the Aral (2, blue line) and Caspian seas (4, orange line).

A comparison of the presented data for two different regions, separated by a considerable distance (2700–3000 km), makes it possible to hypothesize about the existence of similar teleconnections, the physical basis of which may be the features of phenological phases of ice cover revealed from SMOS satellite data by microwave remote sensing methods.

Heat and moisture exchange between two distant territories is possible as a result of winds, the speed and direction of which depend on atmospheric pressure and the temperature of the underlying surface. Figures 7 and 8 show graphs of long-term and monthly wind dynamics recorded at meteorological stations in Western Siberia from the Kara Sea to the Aral Sea: M.V. Popov meteorological station No. 20667 (M1: Bely Island); No. 23330 (M2: Salekhard); No. 28367 (M3: Tyumen); and No. 35746 (M4: Aralsk). Meteorological data was obtained from the www.meteo.ru (accessed on 25 December 2025) (M1–M3) and www.rp5.ru (accessed on 25 December 2025) (M4) datasets.

Figure 1 shows the locations of meteorological stations in Western Siberia; their data were used to calculate the proportion of north–south and south–north winds. In this case, wind is considered as the atmospheric transport of heat (thermal waves) from south to north and moisture from north to south.

Figure 7 shows that, from 1965 to 2025, the proportion of south-to-north winds recorded at the M.V. Popov meteorological station (Bely Island) increased from 10 to 15%, despite annual fluctuations reaching 3–5% in some years.

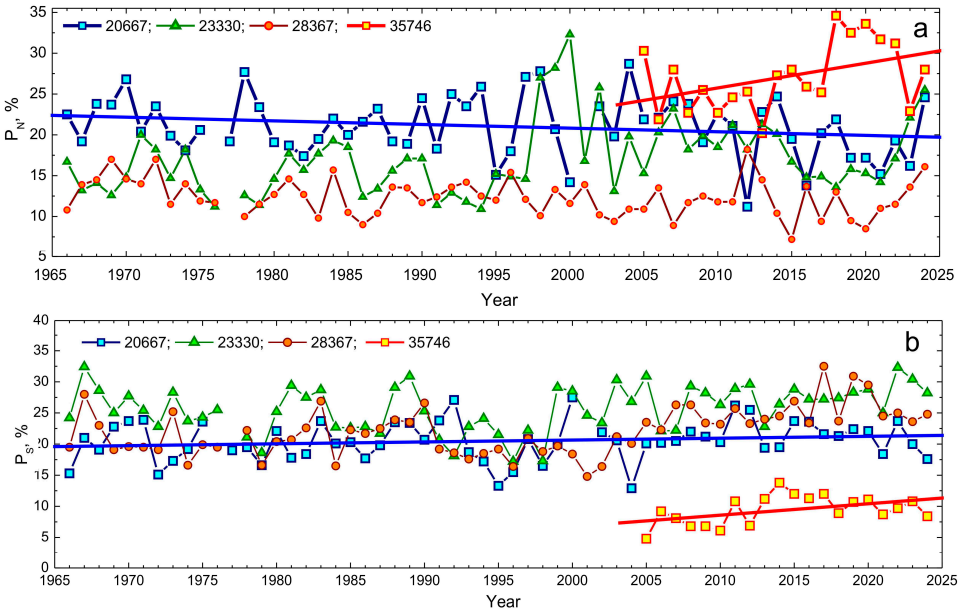

Figure 7. Percentages of northern (**a**) and southern (**b**) winds recorded at weather stations ($P_{N'}$ % and $P_{S'}$ % accordingly): 20667—Popov Polar Station, Bely Island (M1); 23330—Salekhard (M2); 28367—Tyumen (M3); and 35746—Aralsk (M4) by year. Lines without symbols represent statistically significant linear regressions between P and year. (**a**) Station 20667, P = 0.12; station 35746, P = 0.056; (**b**) station 20667, P = 0.22; station 35746, P = 0.04.

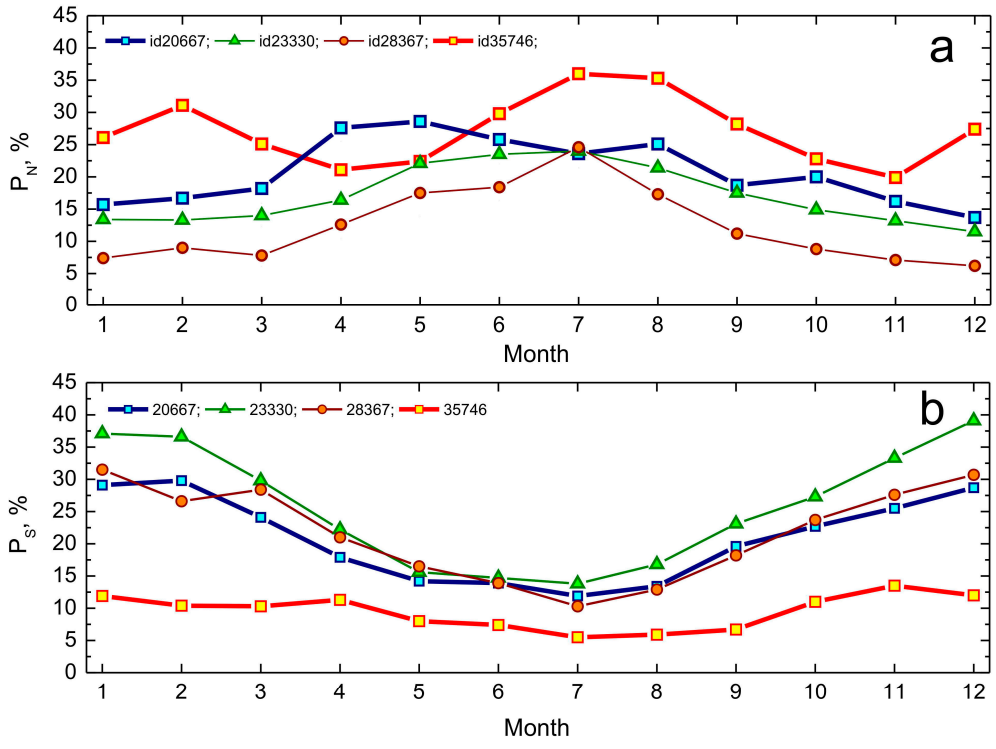

Figure 8. Percentages of northern (**a**) and southern (**b**) winds recorded at weather stations ($P_{N'}$ % and $P_{S'}$ % accordingly) 20667—Popov Polar Station (M1), Bely Island; 23330—Salekhard (M2); 28367—Tyumen (M3); 35746—Aralsk (M4) by month.

Analysis of the seasonal distribution of all winds throughout the year suggests the occurrence of the majority of all southerly winds blowing in a northerly direction during the cold months. The majority of all northerly winds blow in a southerly direction during the warm season (summer). Accordingly, during the cold season, northerly winds transport

moisture southward, while in the summer months, southerly winds (hot, dry winds), including those blowing from the Aralkum Desert, carry heat (heat waves) to northern latitudes, which can "warm" northern territories. Thus, a year-round mechanism of heat transfer from south to north and moisture from north to south emerges.

At the same time, the proportion of northerly winds blowing south, as measured at weather station No. 20667 (Bely Island), fluctuates significantly, ranging from 5% to 20%. Moreover, the duration of open water in the Kara Sea is inversely proportional to the proportion of winds blowing from higher latitudes (from the Arctic Ocean) to the south. This is quite understandable as the more winds blowing from higher latitudes (with lower temperatures), the shorter the warm period, the faster the Kara Sea freezes over, and the longer the freeze-up period. However, a similar situation is observed in the Caspian and Aral Seas, located much further south. Similar trends are observed at other weather stations. The proportion of north–south winds varies between 15% and 28%. The figure shows that the number of winds blowing from north to south in 2012 (the most severe drought for the period of 1965–2025) was the lowest since 1965.

Figure 7a shows the long-term dynamics of winds blowing from the north in a southerly direction (P_N). Figure 7b shows the dynamics of winds blowing from the south in a northerly direction (P_S). These figures also show the long-term trends for the northern weather station 20667 and the southern weather station 35746 (Aralsk) in the vicinity of the Aral Sea. From Figure 7a it is evident that the proportion of (P_N) winds recorded at weather station 20667 is decreasing. At the same time, the proportion of winds blowing from southerly directions to the north is increasing (Figure 7b). The proportion of winds blowing from the south in a northerly direction recorded at weather station 35746 is also increasing. This is especially important as it could increase the frequency and number of heat waves carried from the south of Northern Eurasia to the northern regions.

Figure 8a,b shows the monthly dynamics of P_N and P_S. As in Figure 7a,b, the northern (20667) and southern (35746) meteorological stations are highlighted for comparison. The maximum of the northern winds (P_N) blowing from the Kara Sea (20667) occurs in the spring months (April–May), and the minimum occurs in the summer months (June–August). For the southern territories of Northern Eurasia (according to 35746), the distribution pattern of P_N is completely different (Figure 8a), with two maxima in February and July–August. The share of southern winds P_S (35746) also has two weakly expressed maxima in April and November. The experimental data presented suggest that the maximum and minimum winds from the north and south occur at different times of the year. The observed distribution of P_S (Figure 8b), recorded at weather stations 20667 and 35746, may indicate an increase in heat waves from September to November, which could well trigger an extension of the open-water period in the Kara Sea during the autumn–winter period.

4. Discussion

Our study compared hydrological changes in two very different regions of Northern Eurasia, the Arctic seas and the inland Aral Sea area, showing different dynamics but similar trends in the cyclicity of open-water periods. Although hydrological changes in the two areas have been described earlier, particularly the retreat of Arctic sea ice [117] and the drying of the Aral Sea [118], we hypothesized that the changes were linked by environmental teleconnections and then used new remote sensing approaches and meteorological data to show that each region potentially influences the other, thereby demonstrating likely teleconnections over approximately 2700–3000 km. Depending on wind speed and direction, the transfer of atmospheric heat and moisture between northern and southern regions can take from 3 to 6 days according to the Beaufort scale.

Assessing the possible mutual influences of hydrological changes occurring in different regions located in the north and south of Northern Eurasia is a complex multifactorial ecological and social problem with far-reaching economic and political consequences. The scale of potential damage as a result of hydrological change may cause a significant systemic risk to the future well-being of the population and ecosystems [119] of both regions. Consequently, it is important to explore changes in each region in more detail and to explore if and how changes in one region could affect the other.

4.1. Refined Analyses of Changes in the Kara Sea Region

A decrease in the severity of winter conditions for the Kara Sea area is associated with an increased duration of the open-water period in summer and a proportional reduction in the duration of the freeze-up period in winter. The rate of Kara Sea ice loss (and ice loss in the Arctic Ocean as a whole) is accelerating in the summer period, primarily due to rising air temperatures. Ice cover during the winter period has also significantly decreased, and the ratio of different forms of ice has also changed.

We looked in greater detail at the major phases of the ice regime. The daily data from SMOS (L1C) bound to the DGG ISEA 4H9 enable us to estimate seasonal dynamics of the brightness temperature of the sea surface. Based on the analysis of dependences $T_{\mathrm{BH}}(JD)$, the major phases of the ice regime in the marine area have been established. The duration of OWP determined from dependence on $T_{\mathrm{BH}}(JD)$ is used as a radiophysical criterion for remote assessment of hydrological changes in Northern Eurasia. A promising new criterion is the duration of ice formation, which characterizes the severity of weather conditions.

From the analysis of long-term seasonal dynamics of brightness temperature $T_{\mathrm{BH}}(JD)$ (JD—the Julian day JD counted from the beginning of the observation period 1 January 2012) for the Kara Sea, using SMOS satellite data, we found that the duration of open water experiences cyclical variations. In turn, we expect that an increase/decrease in the duration of open-water periods will lead to a possible increase/decrease in the volume of water evaporating from the waters of these seas. This may lead to a disruption of established hydrological regimes, consisting of a change in the duration of the summer and winter seasons, a redistribution of seasonal precipitation, an increase in the duration of open water periods, and shifts in the beginning and end of ice formation.

4.2. Refined Analyses of Changes in the Aral Sea Area

The Aralkum Desert (now more than 38 thousand square kilometers) is located in Central Asia where desertification processes result in the catastrophic drying up of the AS. The main causes of desertification are the overall decrease and seasonal redistribution of precipitation in the region, an increase in the temperature of the underlying surface, an increase in the duration of dry periods, and soil salinization as a result of wind transfer of toxic salts. The area of the Aral Sea decreased from 68,000 km^2 in the 1960s to 5130 km^2 in 2025 (a more than 13-fold reduction). As a result of many years of drying out, the Aral Sea broke up into two separate basins—the North Aral Sea and the South Aral Sea—with the latter subsequently breaking up into the West Basin and East Basin.

As a result of particularly strong drying out in 2009 and 2014, the East Basin almost completely dried up within a few months, leaving behind an exposed bed. This led to more frequent dust storms, and the formation of large amounts of salty dust, which poses a serious threat to the environment and human health, vegetation degradation and, as a result, an expansion of desertification and a significant deterioration of the environment.

Our new, detailed analysis of long-term seasonal dynamics of BT showed long-term stability for the northern part of the Caspian Sea, the steppe between the Caspian and Aral Seas, the hypersaline Lake Sarykamysh, the western part of the Aral Sea, and the Northern

Aral Sea. However, BT has increased since 2020 due to the salt marsh formed as a result of the drying out of the former basin of the Aral Sea. Our detailed analysis also highlighted a 4-year cyclicity in the duration of the open-water period (2012–2025) for the Aral Sea, which was synchronized with the cyclicities for the Kara, Barents, and Caspian Seas.

4.3. Possible Teleconnections Between Changes in the Kara and Barents Sea Areas

We have presented data on wind directions from each region that shows possible teleconnection mechanisms for the transport of heat and moisture. From 2005 to 2025, the proportion of south-to-north winds recorded on Bely Island (on the coast of the Kara Sea) in the north, increased from 10 to 15%. During the warm season, heat waves propagate northward from the Aral Sea area on these dry winds. This leads to the faster heating of the tundra and the water surfaces of marginal seas, which contributes to an extension of the open-water period in the Kara Sea. In turn, the increased duration of the open-water period leads to more precipitation evaporating and being transported southward by northerly winds in the cold season. These cold winds, laden with moisture, contribute to the humidification of southern territories. This transport of moisture (both rain and snow) from north to south will slow the aridization of the southern environment, and, in particular, could slow or stop the expansion of the Aralkum Desert. The process could also extend winter and reduce spring temperatures because of increased snow fall from the northern winds.

Thus, a year-round mechanism of heat transfer from south to north and moisture from north to south emerges.

The intensification of these hydrological changes that include an increase in heat-carrying dry winds, can potentially result in the transport of fine dust with toxic salts from the surface of Aralkum to both the southern and northern regions of Western Siberia. Consequently, the areas of saline soils could increase, the salinity of water of inland reservoirs could increase, and, accordingly, the freezing temperature could decrease, the periods of open water increase, and the periods of ice decrease. The reduction in the periods of ice, the increase in water salinity, and the decrease in the freezing temperature could lead to an increase in the amount of evaporated moisture, the atmospheric transfer of which to the southern regions of Northern Eurasia could contribute to an increase in the amount of winter precipitation, an increased accumulation of snow reserves in the southern regions, and an increase in the likelihood of catastrophic floods.

4.4. Possible Implications of Changes in the Aral Sea Area for Other Regions

In the middle latitudes, between the Kara Sea and the Aral Sea, hydrological changes are manifested in the drying up of large mineral lakes (Kulundinskoye, Chany, the system of lakes Bolshoy and Maly Azhbulat, etc.) and the drying up of small, highly mineralized lakes with the formation of salt marshes in their place [120–126]. There may be a connection between warm dry winds blowing from the surface of the sandy salt desert of Aralkum, Kulunda, and the Baraba steppes to the north (10–15% of all winds) with a reduction in the periods of freeze-up and a decrease in the area of perennial ice, a probable increase in the salinity of the ice cover, and a decrease in its melting temperature. It has already been reported [127] that fine dust from the surface of the sandy and salty Aralkum desert can reach the Arctic Ocean.

The contribution of distant and ultra-distant sources of dust pollution in the coastal areas of the Kara Sea in the winter–spring period has also been recorded [128].

4.5. Societal Impacts

More than 10 million people live in the territory of Western Siberia and Central Asia where we expect the teleconnections to operate. Hydrological and climatic changes occur-

ring in these macroregions already have a negative impact on the socio-economic activities of most of the population and any teleconnections will exacerbate these impacts [121,122].

The social consequences of the drought in the south (in the Aral Sea region) are already large-scale and serious [129–131]. For example, farmers in the region, for whom agriculture is the main source of livelihood and income, are suffering from droughts, expanding salinized areas, and declining water resources for irrigation. Decreasing agricultural income due to declining soil fertility and a lack of access to safe water and food is forcing some residents to migrate to other settlements outside the region. All these negative social processes will intensify with hydrological and climatic instability.

In the northern regions, there are small populations of the Indigenous Peoples of the North. Their main economic activities are reindeer herding, hunting, and fishing. The alternation of periods of open water and ice-free tundra can lead to significant problems in cases where the tundra is swampy, waterlogged, and impassable for most of the year. Any ecological changes could affect their food and water sources and well-being.

Considering the potential adverse hydrological effects and societal challenges of changes in our two study regions, and the possible teleconnections between them, we propose that it is now important to test our hypotheses. Demonstrating teleconnections and understanding their impacts are important to forewarn those local populations that are likely to be affected. Possible future investigations could focus on tracking wind directions and isotopic analysis of dust and salt transported in the atmosphere to detect their origins, as well as the remote sensing of the direction of hydrological change processes.

5. Conclusions

Our main goal was to explore concurrent changes in the Kara and Aral Sea areas and to construct testable hypotheses on how these two distant areas could affect each other. Our novel results show that the following:

1. The studied long-term seasonal dynamics of the brightness temperature (L-band) of the underlying surface for test sites in the catastrophically shriveled Aral Sea and the resulting Aralkum Desert indicate ongoing aridization of the area.
2. Long-term trends in radiophysical criteria can be used in forecasting climate changes in Northern Eurasia to reduce impacts such as possible economical losses and minimize other social consequences of environmental changes.
3. The mechanisms of proposed mutual influence of hydrological and climatic changes in the northern and southern regions of Northern Eurasia are very diverse, as shown by exploring changes in hydrology in two very different areas of Northern Eurasia—the Arctic seas and the inland Aral Sea area.
4. This information has been used to hypothesize how hydrological changes in one region affect the other, and we have proposed that wind movements are the mechanisms for the teleconnections. However, these hypothesized causal teleconnections now need to be validated, for example, by investigating radioisotope signatures of precipitation and dust and by incorporating atmospheric circulation model simulations or trajectory tracking analyses to validate the north–south heat and water vapor transport pathways proposed in this study.

This is important because current climate models and climate assessments do not represent the increase in hydrological changes and interconnections that may bias climate change projections and assessments of climate sensitivity. Climate model simulations of future changes in hydrological teleconnections are very uncertain. Further work is thus needed to constrain the connectivity of hydrological changes (north–south and opposite) and their effects on climate, so that society can mitigate them and/or adapt to them.

One important question remains: can we reverse these processes? To what extent must the Arctic warm, and how must the annual precipitation distribution and wind direction change, for the Arctic to cease being cold and for Central Asia to cease being hot?

Author Contributions: Conceptualization, T.V.C. and A.N.R.; methodology, A.N.R., I.V.K., I.V.R., and V.V.T.; software, I.V.K. and I.V.R.; validation, I.V.K., I.V.R., and V.V.T.; formal analysis, T.V.C., I.V.K., I.V.R., V.V.T., and O.M.S.; investigation, T.V.C., A.N.R., I.V.K., I.V.R., V.V.T., and O.M.S.; resources, T.V.C., A.N.R., I.V.K., I.V.R., V.V.T., and O.M.S.; data curation, I.V.K. and I.V.R.; writing—original draft preparation, A.N.R., I.V.K., I.V.R., V.V.T., and O.M.S.; writing—review and editing, T.V.C., V.V.T., and O.M.S.; visualization, I.V.K. and I.V.R.; supervision, T.V.C. and A.N.R.; project administration, T.V.C. and O.M.S.; funding acquisition, T.V.C. All authors have read and agreed to the published version of the manuscript.

Funding: This research was carried out within the framework of the state assignment of the Institute of Water and Environmental Problems SB RAS (FUFZ-2026-0003), Space Research Institute Russian Academy of Sciences topic "Monitoring" (State Registration no. 122042500031-8). The study was also supported by the Development Program of Tomsk State University ("Priority-2030"), project no.2.2.1.24 SRG.

Data Availability Statement: The original contributions presented in this study are included in the article. Further inquiries can be directed to the corresponding authors.

Acknowledgments: All coauthors thank all the reviewers for constructive comments. The study is a contribution to the Siberian Environmental Change Network (SECNet) and the authors are grateful to SECNet partners for their cooperation.

Conflicts of Interest: The authors declare no conflicts of interest. The funders had no role in the design of the study; in the collection, analyses, or interpretation of data; in the writing of the manuscript; or in the decision to publish the results.

Abbreviations

The following abbreviations are used in this manuscript:

λ	Wavelength
BT	Brightness temperature
CICP	Period of complete ice cover
d	Ice cover thickness
DGG	Discrete geodetic grid
EB	East Basin of the SAS
ICFP	Period of ice cover formation
ICDP	Period of ice cover destruction
ISEA	Icosahedral Snyder equal area
JD	Julian day
L	Skin layer thickness
MODIS	Moderate-Resolution Imaging Spectroradiometer
NAS	North Aral Sea
OWP	open-water period
P_N	Percentages of northern winds
P_S	Percentages of southern winds
S	Salinity
SAS	South Aral Sea
SFS	Seasonally frozen soils
SMOS	Soil Moisture and Ocean Salinity
T	Temperature
WB	West Basin of the SAS

References

1. Bjerke, J.W.; López-Blanco, E.; Tømmervik, H.; Striberny, A.; Davids, C.; Ólafsdóttir, R.; Karlsen, S.R.; Sandström, P.; Turunen, M.; Rikkonen, T.; et al. Nordic Boreo-Arctic Lands under Rapid Climatic Change: A Review of Recent and Future Trends and Extreme Events. *Earth Sci. Rev.* **2025**, *261*, 105012. [CrossRef]
2. Ogunrinde, A.T.; Xian, X.; Adigun, P.; Adawa, I.S.; Zhao, D.; Xing, Z.; Temitope, I.J. Assessing Teleconnection Influences on the Spatial and Temporal Patterns of Meteorological Drought in Northwest China. *Big Earth Data* **2024**, *8*, 703–731. [CrossRef]
3. Zhou, W.; Leung, L.R.; Lu, J. Steady threefold Arctic amplification of externally forced warming masked by natural variability. *Nat. Geosci.* **2024**, *17*, 508–515. [CrossRef]
4. Phoenix, G.K.; Bjerke, J.W.; Björk, R.G.; Blok, D.; Bryn, A.; Callaghan, T.V.; Christiansen, C.T.; Cunliffe, A.M.; Davidson, S.J.; Epstein, H.E.; et al. Browning Events in Arctic Ecosystems: Diverse Causes with Common Consequences. *PLoS Clim.* **2025**, *4*, e0000570. [CrossRef]
5. Callaghan, T.V.; Cazzolla Gatti, R.; Phoenix, G. The Need to Understand the Stability of Arctic Vegetation during Rapid Climate Change: An Assessment of Imbalance in the Literature. *Ambio* **2022**, *51*, 1034–1044. [CrossRef] [PubMed]
6. Harris, C.; Arenson, L.U.; Christiansen, H.H.; Etzelmüller, B.; Frauenfelder, R.; Gruber, S.; Haeberli, W.; Hauck, C.; Hölzle, M.; Humlum, O.; et al. Permafrost and Climate in Europe: Monitoring and Modelling Thermal, Geomorphological and Geotechnical Responses. *Earth-Sci. Rev.* **2009**, *92*, 117–171. [CrossRef]
7. Bring, A.; Destouni, G. Hydro-Climatic Changes and Their Monitoring in the Arctic: Observation-Model Comparisons and Prioritization Options for Monitoring Development. *J. Hydrol.* **2013**, *492*, 273–280. [CrossRef]
8. Karlsson, J.M.; Jaramillo, F.; Destouni, G. Hydro-Climatic and Lake Change Patterns in Arctic Permafrost and Non-Permafrost Areas. *J. Hydrol.* **2015**, *529*, 134–145. [CrossRef]
9. Karjalainen, O.; Aalto, J.; Luoto, M.; Westermann, S.; Romanovsky, V.E.; Nelson, F.E.; Etzelmüller, B.; Hjort, J. Circumpolar Permafrost Maps and Geohazard Indices for Near-Future Infrastructure Risk Assessments. *Sci. Data* **2019**, *6*, 190037. [CrossRef] [PubMed]
10. Liu, Q.; Piao, S.; Janssens, I.A.; Fu, Y.; Peng, S.; Lian, X.; Ciais, P.; Myneni, R.B.; Peñuelas, J.; Wang, T. Extension of the Growing Season Increases Vegetation Exposure to Frost. *Nat. Commun.* **2018**, *9*, 426. [CrossRef]
11. Intergovernmental Panel on Climate Change (IPCC). Climate Change 2022–Mitigation of Climate Change: Working Group III Contribution to the Sixth Assessment Report of the Intergovernmental Panel on Climate Change. In *Intergovernmental Panel on Climate Change (Ipcc)*, 1st ed.; Cambridge University Press: Cambridge, UK, 2023; ISBN 978-1-009-15792-6. [CrossRef]
12. Callaghan, T.V.; Shaduyko, O.; Kirpotin, S.N.; Gordov, E. Siberian Environmental Change: Synthesis of Recent Studies and Opportunities for Networking. *Ambio* **2021**, *50*, 2104–2127. [CrossRef]
13. Haustein, K.; Allen, M.R.; Forster, P.M.; Otto, F.E.L.; Mitchell, D.M.; Matthews, H.D.; Frame, D.J. A Real-Time Global Warming Index. *Sci. Rep.* **2017**, *7*, 15417. [CrossRef]
14. Loginov, V.F.; Brovka, Y.A. Periods of domination of the influence of natural and anthropogenic factors on climate. *Hydrosphere Hazard. Process. Phenom.* **2023**, *4*, 381–400. [CrossRef]
15. Serreze, M.C.; Barry, R.G. Processes and Impacts of Arctic Amplification: A Research Synthesis. *Glob. Planet. Change* **2011**, *77*, 85–96. [CrossRef]
16. Anisimov, O.; Kokorev, V.; Zhiltcova, Y. Arctic Ecosystems and Their Services Under Changing Climate: Predictive-Modeling Assessment. *Geogr. Rev.* **2017**, *107*, 108–124. [CrossRef]
17. Mudryk, L.; Santolaria-Otín, M.; Krinner, G.; Ménégoz, M.; Derksen, C.; Brutel-Vuilmet, C.; Brady, M.; Essery, R. Historical Northern Hemisphere Snow Cover Trends and Projected Changes in the CMIP6 Multi-Model Ensemble. *Cryosphere* **2020**, *14*, 2495–2514. [CrossRef]
18. Sato, T.; Nakamura, T.; Iijima, Y.; Hiyama, T. Enhanced Arctic Moisture Transport toward Siberia in Autumn Revealed by Tagged Moisture Transport Model Experiment. *NPJ Clim. Atmos. Sci.* **2022**, *5*, 91. [CrossRef]
19. Callaghan, T.V.; Johansson, M.; Brown, R.D.; Groisman, P.Y.; Labba, N.; Radionov, V.; Bradley, R.S.; Blangy, S.; Bulygina, O.N.; Christensen, T.R.; et al. Multiple Effects of Changes in Arctic Snow Cover. *Ambio* **2011**, *40*, 32–45. [CrossRef]
20. Ramage, J.; Jungsberg, L.; Wang, S.; Westermann, S.; Lantuit, H.; Heleniak, T. Population Living on Permafrost in the Arctic. *Popul. Environ.* **2021**, *43*, 22–38. [CrossRef]
21. CBD (Convention on Biological Diversity). *First Draft of the Post-2020 Global Biodiversity Framework*; CBD: Montreal, QC, Canada, 2021.
22. Loreau, M.; Hector, A.; Isbell, F. *The Ecological and Societal Consequences of Biodiversity Loss*; ISTE: Arlington, VI, USA; John Wiley & Sons: Hoboken, NJ, USA, 2022; 384p, ISBN 978-1-119-90290-4.
23. Amirkhanov, A.M.; Zhukov, M.A.; Kershengolts, B.M.; Okhlopkov, I.M.; Romanenkov, R.L.; Sapogin, A.A.; Tishkov, A.A.; Ustinova, T.V. *Conservation of Biodiversity in the Arctic. Problems, Tasks, Solutions*; Fizmatkniga: Moscow, Russia, 2023; 139p, ISBN 978-5-89155-778-9.
24. Stroeve, J.; Notz, D. Changing State of Arctic Sea Ice across All Seasons. *Environ. Res. Lett.* **2018**, *13*, 103001. [CrossRef]

25. Luo, B.; Luo, D.; Dai, A.; Xiao, C.; Simmonds, I.; Hanna, E.; Overland, J.; Shi, J.; Chen, X.; Yao, Y.; et al. Rapid Summer Russian Arctic Sea-Ice Loss Enhances the Risk of Recent Eastern Siberian Wildfires. *Nat. Commun.* **2024**, *15*, 5399. [CrossRef]
26. Liu, G.; Li, J.; Ying, T.; Dong, Y.; Zhang, Z.; Zhang, C.; Li, Q. Beaufort Sea Ice Loss Contributes to Enhanced Health Exposure to Fire Weather over Southeast Asia. *NPJ Clim. Atmos. Sci.* **2025**, *8*, 60. [CrossRef]
27. Li, X.; Jin, H.; Wang, H.; Jin, X.; Bense, V.F.; Marchenko, S.S.; He, R.; Huang, Y.; Luo, D. Effects of Fire History on Thermal Regimes of Permafrost in the Northern Da Xing'anling Mountains, NE China. *Geoderma* **2022**, *410*, 115670. [CrossRef]
28. Alizadeh, M.R.; Adamowski, J.; Entekhabi, D. Land and Atmosphere Precursors to Fuel Loading, Wildfire Ignition and Post-Fire Recovery. *Geophys. Res. Lett.* **2024**, *51*, e2023GL105324. [CrossRef]
29. Kazakova, U.; Polukhin, A.; Shabanov, P. Origin and Evolution of the Surface Desalinated Layer of the Kara Sea during the Ice-Free Period. *J. Mar. Syst.* **2024**, *243*, 103950. [CrossRef]
30. Liu, Y.; Tang, Q.; Zhang, C.; Chen, D.; Francis, J.A.; Leung, L.R.; Chen, H.W. The Disproportionate Impact of Enhanced Evaporation from Melting Arctic Sea Ice on Cold-Season Land Precipitation Trends. *NPJ Clim. Atmos. Sci.* **2024**, *7*, 126. [CrossRef]
31. Wu, H.; Xu, M.; Zhu, M. Changes of Hydrological Components in Arctic Rivers Based on Multi-Source Data during 2003–2016. *Water* **2021**, *13*, 3494. [CrossRef]
32. Xu, C.; Ma, J.-H.; Sun, J.-Q.; You, C.; Ma, Y.-M.; Wang, H.-J.; Wang, T. Links between Winter Dust over the Tibetan Plateau and Preceding Autumn Sea Ice Variability in the Barents and Kara Seas. *Adv. Clim. Change Res.* **2022**, *13*, 896–908. [CrossRef]
33. Kok, J.F.; Storelvmo, T.; Karydis, V.A.; Adebiyi, A.A.; Mahowald, N.M.; Evan, A.T.; He, C.; Leung, D.M. Mineral Dust Aerosol Impacts on Global Climate and Climate Change. *Nat. Rev. Earth Environ.* **2023**, *4*, 71–86. [CrossRef]
34. Groisman, P.; Bulygina, O.; Henebry, G.; Speranskaya, N.; Shiklomanov, A.; Chen, Y.; Tchebakova, N.; Parfenova, E.; Tilinina, N.; Zolina, O.; et al. Dryland Belt of Northern Eurasia: Contemporary Environmental Changes and Their Consequences. *Environ. Res. Lett.* **2018**, *13*, 115008. [CrossRef]
35. Zhou, Y.; Wu, T.; Zhou, Y.; Zhang, J.; Zhang, F.; Su, X.; Jie, W.; Zhao, H.; Zhang, Y.; Wang, J. Can Global Warming Bring More Dust? *Clim. Dyn.* **2023**, *61*, 2693–2715. [CrossRef]
36. Mao, R.; Ho, C.-H.; Shao, Y.; Gong, D.-Y.; Kim, J. Influence of Arctic Oscillation on Dust Activity over Northeast Asia. *Atmos. Environ.* **2011**, *45*, 326–337. [CrossRef]
37. Nakamura, T.; Sato, T. A Possible Linkage of Eurasian Heat Wave and East Asian Heavy Rainfall in Relation to the Rapid Arctic Warming. *Environ. Res.* **2022**, *209*, 112881. [CrossRef]
38. Li, X.; Guo, H.; Cheng, G.; Song, X.; Ran, Y.; Feng, M.; Che, T.; Li, X.; Wang, L.; Duan, A.; et al. Polar Regions Are Critical in Achieving Global Sustainable Development Goals. *Nat. Commun.* **2025**, *16*, 3879. [CrossRef]
39. Tikhonov, V.; Khvostov, I.; Romanov, A.; Sharkov, E. Theoretical Study of Ice Cover Phenology at Large Freshwater Lakes Based on SMOS MIRAS Data. *Cryosphere* **2018**, *12*, 2727–2740. [CrossRef]
40. Boyarskii, D.A.; Romanov, A.N.; Khvostov, I.V.; Tikhonov, V.V.; Sharkov, E.A. On Evaluating the Depth of Soil Freezing Based on SMOS Satellite Data. *Izv. Atmos. Ocean. Phys.* **2019**, *55*, 996–1004. [CrossRef]
41. Zhurbas, N.V.; Zavialov, P.O. Effect of Stratification on Wind Drift of River Runoff in the Kara Sea. *Oceanology* **2015**, *55*, 827–831. [CrossRef]
42. Romanov, A.N. Relationship between Seasonal Variations in Radio-Brightness Temperatures in the Kara Sea Area and Hydrological-Climate Changes in the Arctic. *Russ. Phys. J.* **2023**, *66*, 34–47, (In Russian with English Abstract).
43. Cai, Q.; Wang, J.; Beletsky, D.; Overland, J.; Ikeda, M.; Wan, L. Accelerated Decline of Summer Arctic Sea Ice during 1850–2017 and the Amplified Arctic Warming during the Recent Decades. *Environ. Res. Lett.* **2021**, *16*, 034015. [CrossRef]
44. Matveeva, T.A.; Semenov, V.A.; Astafyeva, E.S. Arctic sea ice coverage and its relation to the surface air temperature in the Northern Hemisphere. *Ice Snow* **2020**, *60*, 134–148, (In Russian with English Abstract). [CrossRef]
45. Murmansk Marine Biological Institute of the Russian Academy of Sciences; Bulavina, A.S. The Effect of Fluctuations of the Ob and Yenisei Rivers Runoff on the Area of the Kara Sea Ice Cover. *TKSC RAS NSH* **2023**, *2*, 10–18. [CrossRef]
46. Naumov, L.; Gordeeva, S. Variability of Ice in the Kara Sea. 2023. Available online: https://www.researchgate.net/publication/371349282_Izmencivost_ledovitosti_Karskogo_mora (accessed on 1 September 2025).
47. Istomin, E.P.; Petrov, Y.A.; Martyn, I.A.; Novozhilova, E.S. Assessment of the Variability of Climatic Characteristics of the Kara Sea for the Safe and Efficient Use of the Northern Sea Route. *Geoinformatika* **2024**, *2*, 45–53. (In Russian) [CrossRef]
48. Guo, H.; Bao, A.; Liu, T.; Jiapaer, G.; Ndayisaba, F.; Jiang, L.; Kurban, A.; De Maeyer, P. Spatial and Temporal Characteristics of Droughts in Central Asia during 1966–2015. *Sci. Total Environ.* **2018**, *624*, 1523–1538. [CrossRef]
49. Russell, A.; Ghalaieny, M.; Gazdiyeva, B.; Zhumabayeva, S.; Kurmanbayeva, A.; Akhmetov, K.K.; Mukanov, Y.; McCann, M.; Ali, M.; Tucker, A.; et al. A Spatial Survey of Environmental Indicators for Kazakhstan: An Examination of Current Conditions and Future Needs. *Int. J. Environ. Res.* **2018**, *12*, 735–748. [CrossRef]
50. Sharma, A.; Huang, H.-P.; Zavialov, P.; Khan, V. Impact of Desiccation of Aral Sea on the Regional Climate of Central Asia Using WRF Model. *Pure Appl. Geophys.* **2018**, *175*, 465–478. [CrossRef]

51. Jiang, L.; Jiapaer, G.; Bao, A.; Kurban, A.; Guo, H.; Zheng, G.; De Maeyer, P. Monitoring the Long-Term Desertification Process and Assessing the Relative Roles of Its Drivers in Central Asia. *Ecol. Indic.* **2019**, *104*, 195–208. [CrossRef]
52. Jiang, L.; Jiapaer, G.; Bao, A.; Li, Y.; Guo, H.; Zheng, G.; Chen, T.; De Maeyer, P. Assessing Land Degradation and Quantifying Its Drivers in the Amudarya River Delta. *Ecol. Indic.* **2019**, *107*, 105595. [CrossRef]
53. Karimov, B.K.; Matthies, M.; Talskikh, V.; Plotsen, M.A.; Karimov, E.B. Salinization of River Waters and Suitability of Electric Conductivity Value for Saving Freshwater from Salts in Aral Sea Basin. *Asian J. Water Environ. Pollut.* **2019**, *16*, 109–114. [CrossRef]
54. Micklin, P. The future Aral Sea: Hope and despair. *Environ. Earth Sci.* **2016**, *75*, 844. [CrossRef]
55. Varotsos, C.A.; Krapivin, V.F.; Mkrtchyan, F.A. On the Recovery of the Water Balance. *Water Air Soil. Pollut.* **2020**, *231*, 170. [CrossRef]
56. Database of the Aral Sea. Available online: https://www.cawater-info.net/aral/data/monitoring_amu_e.htm (accessed on 10 September 2025).
57. Singh, A.; Behrangi, A.; Fisher, J.B.; Reager, J.T. On the Desiccation of the South Aral Sea Observed from Spaceborne Missions. *Remote Sens.* **2018**, *10*, 793. [CrossRef]
58. Luo, S.; Song, C.; Liu, K.; Ke, L.; Ma, R. An Effective Low-Cost Remote Sensing Approach to Reconstruct the Long-Term and Dense Time Series of Area and Storage Variations for Large Lakes. *Sensors* **2019**, *19*, 4247. [CrossRef]
59. Zhang, J.; Chen, Y.; Li, Z.; Song, J.; Fang, G.; Li, Y.; Zhang, Q. Study on the Utilization Efficiency of Land and Water Resources in the Aral Sea Basin, Central Asia. *Sustain. Cities Soc.* **2019**, *51*, 101693. [CrossRef]
60. Zhou, C.; Gui, H.; Hu, J.; Ke, H.; Wang, Y.; Zhang, X. Detection of New Dust Sources in Central/East Asia and Their Impact on Simulations of a Severe Sand and Dust Storm. *JGR Atmos.* **2019**, *124*, 10232–10247. [CrossRef]
61. Issanova, G.; Abuduwaili, J.; Galayeva, O.; Semenov, O.; Bazarbayeva, T. Aeolian Transportation of Sand and Dust in the Aral Sea Region. *Int. J. Environ. Sci. Technol.* **2015**, *12*, 3213–3224. [CrossRef]
62. Indoitu, R.; Kozhoridze, G.; Batyrbaeva, M.; Vitkovskaya, I.; Orlovsky, N.; Blumberg, D.; Orlovsky, L. Dust Emission and Environmental Changes in the Dried Bottom of the Aral Sea. *Aeolian Res.* **2015**, *17*, 101–115. [CrossRef]
63. Löw, F.; Navratil, P.; Kotte, K.; Schöler, H.F.; Bubenzer, O. Remote-Sensing-Based Analysis of Landscape Change in the Desiccated Seabed of the Aral Sea—A Potential Tool for Assessing the Hazard Degree of Dust and Salt Storms. *Environ. Monit. Assess.* **2013**, *185*, 8303–8319. [CrossRef]
64. Breckle, S.-W.; Wucherer, W. The Aralkum, a Man-Made Desert on the Desiccated Floor of the Aral Sea (Central Asia): General Introduction and Aims of the Book. In *Aralkum–A Man-Made Desert*; Breckle, S.-W., Wucherer, W., Dimeyeva, L.A., Ogar, N.P., Eds.; Ecological Studies; Springer: Berlin/Heidelberg, Germany, 2012; Volume 218, pp. 1–9, ISBN 978-3-642-21116-4.
65. Massakbayeva, A.; Abuduwaili, J.; Bissenbayeva, S.; Issina, B.; Smanov, Z. Water Balance of the Small Aral Sea. *Environ. Earth Sci.* **2020**, *79*, 75. [CrossRef]
66. Ayzel, G.; Izhitskiy, A. Climate Change Impact Assessment on Freshwater Inflow into the Small Aral Sea. *Water* **2019**, *11*, 2377. [CrossRef]
67. Sun, F.; Ma, R. Hydrologic Changes of Aral Sea: A Reveal by the Combination of Radar Altimeter Data and Optical Images. *Ann. GIS* **2019**, *25*, 247–261. [CrossRef]
68. Makkaveev, P.N.; Gordeev, V.V.; Zav'yalov, P.O.; Polukhin, A.A.; Khlebopashev, P.V.; Kochenkova, A.I. Hydrochemical Characteristics of the Aral Sea in 2012–2013. *Water Resour* **2018**, *45*, 188–198. [CrossRef]
69. Samarkhanov, K.; Abuduwaili, J.; Samat, A.; Issanova, G. The Spatial and Temporal Land Cover Patterns of the Qazaly Irrigation Zone in 2003–2018: The Case of Syrdarya River's Lower Reaches, Kazakhstan. *Sustainability* **2019**, *11*, 4035. [CrossRef]
70. Shen, H.; Abuduwaili, J.; Ma, L.; Samat, A. Remote Sensing-Based Land Surface Change Identification and Prediction in the Aral Sea Bed, Central Asia. *Int. J. Environ. Sci. Technol.* **2019**, *16*, 2031–2046. [CrossRef]
71. Löw, F.; Prishchepov, A.V.; Waldner, F.; Dubovyk, O.; Akramkhanov, A.; Biradar, C.; Lamers, J.P.A. Mapping Cropland Abandonment in the Aral Sea Basin with MODIS Time Series. *Remote Sens.* **2018**, *10*, 159. [CrossRef]
72. Gabarro, C.; Turiel, A.; Elosegui, P.; Pla-Resina, J.A.; Portabella, M. New Methodology to Estimate Arctic Sea Ice Concentration from SMOS Combining Brightness Temperature Differences in a Maximum-Likelihood Estimator. *Cryosphere* **2017**, *11*, 1987–2002. [CrossRef]
73. Alekseeva, T.; Tikhonov, V.; Frolov, S.; Repina, I.; Raev, M.; Sokolova, J.; Sharkov, E.; Afanasieva, E.; Serovetnikov, S. Comparison of Arctic Sea Ice Concentrations from the NASA Team, ASI, and VASIA2 Algorithms with Summer and Winter Ship Data. *Remote Sens.* **2019**, *11*, 2481. [CrossRef]
74. Tikhonov, V.V.; Raev, M.D.; Sharkov, E.A.; Boyarskii, D.A.; Repina, I.A.; Komarova, N.Y. Satellite Microwave Radiometry of Sea Ice of Polar Regions: A Review. *Izv. Atmos. Ocean. Phys.* **2016**, *52*, 1012–1030. [CrossRef]
75. Kaleschke, L.; Tian-Kunze, X.; Maaß, N.; Mäkynen, M.; Drusch, M. Sea Ice Thickness Retrieval from SMOS Brightness Temperatures during the Arctic Freeze-up Period. *Geophys. Res. Lett.* **2012**, *39*, 2012GL050916. [CrossRef]
76. Chen, W.; Zhou, Y.; Passe, U.; Zhang, T.; Wang, C.; Asrar, G.R.; Li, Q.; Li, H. Improving Estimation of Diurnal Land Surface Temperatures by Integrating Weather Modeling with Satellite Observations. *Remote Sens. Environ.* **2024**, *315*, 114393. [CrossRef]

77. Hu, J.; Tao, T.; Jia, J.; Zhao, T.; Li, Q.; Yu, H. High-Precision Retrieval of Offshore Sea Surface Temperature: A Machine Learning Framework Based on MODIS and in-Situ Measurements. *Infrared Phys. Technol.* **2024**, *137*, 105129. [CrossRef]
78. Weng, F.; Grody, N.C.; Ferraro, R.R.; Zhao, Q.; Chen, C.T. Global Cloud Water Distribution Derived from Special Sensor Microwave Imager/Sounder and Its Comparison with GCM Simulation. *Adv. Space Res.* **1997**, *19*, 407–411. [CrossRef]
79. Kerr, Y.H.; Waldteufel, P.; Richaume, P.; Wigneron, J.P.; Ferrazzoli, P.; Mahmoodi, A.; Al Bitar, A.; Cabot, F.; Gruhier, C.; Juglea, S.E.; et al. The SMOS Soil Moisture Retrieval Algorithm. *IEEE Trans. Geosci. Remote Sens.* **2012**, *50*, 1384–1403. [CrossRef]
80. Kim, H.; Crow, W.; Li, X.; Wagner, W.; Hahn, S.; Lakshmi, V. True Global Error Maps for SMAP, SMOS, and ASCAT Soil Moisture Data Based on Machine Learning and Triple Collocation Analysis. *Remote Sens. Environ.* **2023**, *298*, 113776. [CrossRef]
81. Li, X.; Wigneron, J.-P.; Frappart, F.; Lannoy, G.D.; Fan, L.; Zhao, T.; Gao, L.; Tao, S.; Ma, H.; Peng, Z.; et al. The First Global Soil Moisture and Vegetation Optical Depth Product Retrieved from Fused SMOS and SMAP L-Band Observations. *Remote Sens. Environ.* **2022**, *282*, 113272. [CrossRef]
82. Faryadi, M. Soil Security under Salt Attack: Protection of the Soil against the Salinization Caused by Drying up of Lake Urmia. *Soil Secur.* **2023**, *13*, 100113. [CrossRef]
83. Poursanidis, D.; Chrysoulakis, N. Remote Sensing, Natural Hazards and the Contribution of ESA Sentinels Missions. *Remote Sens. Appl. Soc. Environ.* **2017**, *6*, 25–38. [CrossRef]
84. Belchansky, G. Estimating the Time of Melt Onset and Freeze Onset over Arctic Sea-Ice Area Using Active and Passive Microwave Data. *Remote Sens. Environ.* **2004**, *92*, 21–39. [CrossRef]
85. Bareiss, J.; Gorgen, K. Spatial and Temporal Variability of Sea Ice in the Laptev Sea: Analyses and Review of Satellite Passive-Microwave Data and Model Results, 1979 to 2002. *Glob. Planet. Change* **2005**, *48*, 28–54. [CrossRef]
86. Drobot, S.D. Using Remote Sensing Data to Develop Seasonal Outlooks for Arctic Regional Sea-Ice Minimum Extent. *Remote Sens. Environ.* **2007**, *111*, 136–147. [CrossRef]
87. Tikhonov, V.V.; Repina, I.A.; Raev, M.D.; Sharkov, E.A.; Ivanov, V.V.; Boyarskii, D.A.; Alexeeva, T.A.; Komarova, N.Y. A Physical Algorithm to Measure Sea Ice Concentration from Passive Microwave Remote Sensing Data. *Adv. Space Res.* **2015**, *56*, 1578–1589. [CrossRef]
88. Richter, F.; Drusch, M.; Kaleschke, L.; Maaß, N.; Tian-Kunze, X.; Mecklenburg, S. Arctic Sea Ice Signatures: L-Band Brightness Temperature Sensitivity Comparison Using Two Radiation Transfer Models. *Cryosphere* **2018**, *12*, 921–933. [CrossRef]
89. Ballabrera-Poy, J.; Mourre, B.; Garcia-Ladona, E.; Turiel, A.; Font, J. Linear and Non-Linear T–S Models for the Eastern North Atlantic from Argo Data: Role of Surface Salinity Observations. *Deep Sea Res. Part. I Oceanogr. Res. Pap.* **2009**, *56*, 1605–1614. [CrossRef]
90. Talone, M.; Sabia, R.; Camps, A.; Vall-llossera, M.; Gabarró, C.; Font, J. Sea Surface Salinity Retrievals from HUT-2D L-Band Radiometric Measurements. *Remote Sens. Environ.* **2010**, *114*, 1756–1764. [CrossRef]
91. Wigneron, J.-P.; Schwank, M.; Baeza, E.L.; Kerr, Y.; Novello, N.; Millan, C.; Moisy, C.; Richaume, P.; Mialon, A.; Al Bitar, A.; et al. First Evaluation of the Simultaneous SMOS and ELBARA-II Observations in the Mediterranean Region. *Remote Sens. Environ.* **2012**, *124*, 26–37. [CrossRef]
92. McCulloch, M.E.; Spurgeon, P.; Chuprin, A. Have Mid-Latitude Ocean Rain-Lenses Been Seen by the SMOS Satellite? *Ocean Model.* **2012**, *43–44*, 108–111. [CrossRef]
93. Olmedo, E.; Martínez, J.; Turiel, A.; Ballabrera-Poy, J.; Portabella, M. Debiased Non-Bayesian Retrieval: A Novel Approach to SMOS Sea Surface Salinity. *Remote Sens. Environ.* **2017**, *193*, 103–126. [CrossRef]
94. Mulet, S.; Rio, M.-H.; Mignot, A.; Guinehut, S.; Morrow, R. A New Estimate of the Global 3D Geostrophic Ocean Circulation Based on Satellite Data and In-Situ Measurements. *Deep. Sea Res. Part. II Top. Stud. Oceanogr.* **2012**, *77–80*, 70–81. [CrossRef]
95. Yin, X.; Boutin, J.; Martin, N.; Spurgeon, P.; Vergely, J.-L.; Gaillard, F. Errors in SMOS Sea Surface Salinity and Their Dependency on a Priori Wind Speed. *Remote Sens. Environ.* **2014**, *146*, 159–171. [CrossRef]
96. Prakash, S.; Gairola, R.M. Estimation of Sea Surface Salinity in the Tropical Indian Ocean by Synergistic Use of SMOS and RAMA Buoy Data. *Methods Oceanogr.* **2013**, *8*, 33–40. [CrossRef]
97. Umbert, M.; Hoareau, N.; Turiel, A.; Ballabrera-Poy, J. New Blending Algorithm to Synergize Ocean Variables: The Case of SMOS Sea Surface Salinity Maps. *Remote Sens. Environ.* **2014**, *146*, 172–187. [CrossRef]
98. Olmedo, E.; Martínez, J.; Umbert, M.; Hoareau, N.; Portabella, M.; Ballabrera-Poy, J.; Turiel, A. Improving Time and Space Resolution of SMOS Salinity Maps Using Multifractal Fusion. *Remote Sens. Environ.* **2016**, *180*, 246–263. [CrossRef]
99. Brassington, G.B.; Divakaran, P. The Theoretical Impact of Remotely Sensed Sea Surface Salinity Observations in a Multi-Variate Assimilation System. *Ocean. Model.* **2009**, *27*, 70–81. [CrossRef]
100. Hoareau, N.; Umbert, M.; Martínez, J.; Turiel, A.; Ballabrera-Poy, J. On the Potential of Data Assimilation to Generate SMOS-Level 4 Maps of Sea Surface Salinity. *Remote Sens. Environ.* **2014**, *146*, 188–200. [CrossRef]
101. Ulaby, F.T.; Moor, R.K.; Fung, A.K. *Microwave Remote Sensing: Active and Passive*; Artech House: Norwood, MA, USA, 1982; 1645p.
102. Romanov, A.N.; Khvostov, I.V.; Ryabinin, I.V.; Troshkin, D.N.; Romanov, D.A. Remote Microwave Soil Drought Index Considering Dielectric Properties of Soil. *IEEE Trans. Geosci. Remote Sens.* **2023**, *61*, 1–8. [CrossRef]

103. Romanov, A.N.; Khvostov, I.V.; Tikhonov, V.V.; Sharkov, E.A. Assessing Hydrological Changes in Wetland Areas of the Russian Arctic, Subarctic, and Northern Taiga Based on Microwave Remote Sensing Data. *Izv. Atmos. Ocean. Phys.* **2022**, *58*, 1100–1110. [CrossRef]
104. Kerr, Y.H.; Waldteufel, P.; Wigneron, J.-P.; Delwart, S.; Cabot, F.; Boutin, J.; Escorihuela, M.-J.; Font, J.; Reul, N.; Gruhier, C.; et al. The SMOS Mission: New Tool for Monitoring Key Elements of the Global Water Cycle. *Proc. IEEE* **2010**, *98*, 666–687. [CrossRef]
105. Gutierrez, A.; Castro, R.; Vieira, P. SMOS L1 Processor L1c Data Processing Model. SO-DS-DME-L1OP-0009. No. 2.14. 2014. p 80. Available online: https://earth.esa.int/documents/10174/1854456/SMOS_L1c-Data-Processing-Models (accessed on 1 September 2025).
106. Sahr, K.; White, D.; Kimerling, A.J. Geodesic Discrete Global Grid Systems. *Cartogr. Geogr. Inf. Sci.* **2003**, *30*, 121–134. [CrossRef]
107. Romanov, A.N.; Khvostov, I.V. On the Validation of Satellite Microwave Remote Sensing Data under Soil Salinity Conditions. *Izv. Atmos. Ocean. Phys.* **2019**, *55*, 1033–1040. [CrossRef]
108. Romanov, A.N.; Khvostov, I.V.; Ulanov, P.N.; Tikhonov, V.V.; Boyarsky, D.A.; Sharkov, E.A.; Pechkin, A.S.; Zhelezova, E.V. Assessment of Hydrological and Climatic Changes in the Arctic based on Satellite Microwave Sounding Data from the Marginal Seas of the Arctic Ocean and Adjacent Tundra. 2018. Available online: http://conf.rse.geosmis.ru/files/books/2018/6604.htm (accessed on 25 December 2025).
109. Anguelova, M.D.; Gaiser, P.W. Microwave Emissivity of Sea Foam Layers with Vertically Inhomogeneous Dielectric Properties. *Remote Sens. Environ.* **2013**, *139*, 81–96. [CrossRef]
110. Romanov, A.N.; Khvostov, I.V.; Ryabinin, I.V.; Tikhonov, V.V.; Sharkov, E.A. Seasonal and Interannual Dynamics of Radio Brightness Temperatures in the Waters of the Eastern Seas of the Arctic Ocean. 2021. Available online: http://conf.rse.geosmis.ru/files/books/2021/8716.htm (accessed on 25 December 2025).
111. Wadhams, P. The Underside of Arctic Sea Ice Imaged by Sidescan Sonar. *Nature* **1988**, *333*, 161–164. [CrossRef]
112. Anderson, M.R.; Crane, R.G.; Barry, R.G. Characteristics of Arctic Ocean Ice Determined from SMMR Data for 1979: Case Studies in the Seasonal Sea Ice Zone. *Adv. Space Res.* **1985**, *5*, 257–261. [CrossRef]
113. Bardin, M.Y.; Rankova, E.Y.; Samokhina, O.F. About the Temperature Regime at the Earth's Surface in June–July 2016. 2016. Available online: http://www.igras.ru/news/1093 (accessed on 25 December 2025).
114. NASA Analysis Finds July 2016 Is Warmest on Record. 2016. Available online: https://data.giss.nasa.gov/gistemp/news/20160816/ (accessed on 25 December 2025).
115. NOAA National Centers for Environmental Information, Monthly Global Climate Report for July 2016. 2016. Available online: https://www.ncei.noaa.gov/access/monitoring/monthly-report/global/201607/2016-year-to-date-temperatures-versus-previous-years (accessed on 25 December 2025).
116. Troshkin, D.N.; Ryabinin, I.V.; Khvostov, I.V.; Romanov, A.N. Modeling the Characteristics of Agricultural Drought Based on the Gaussian Distribution. 2022. Available online: http://conf.rse.geosmis.ru/files/books/2022/9303.htm (accessed on 25 December 2025). (In Russian)
117. Kwok, R. Arctic Sea Ice Thickness, Volume, and Multiyear Ice Coverage: Losses and Coupled Variability (1958–2018). *Environ. Res. Lett.* **2018**, *13*, 105005. [CrossRef]
118. Jabbarov, Z.; Kholdorov, S.; Nomozov, U.; Makhammadiev, S.; Djalilova, G.; Abdullaev, S. The Drying of the Aral Sea: Soil Formation and Restoration Potential on the Seabed. *Soil Sci. Annu.* **2025**, *76*, 1–12. [CrossRef]
119. Kumar, A. Challenge of Climate Change. In *Ecosystem-Based Adaptation*; Elsevier: Amsterdam, The Netherlands, 2022; pp. 39–104, ISBN 978-0-12-815025-2.
120. Novikova, N.M. Ecological and Geographical Aspects of the Aral Sea Crisis. Part 2. Research of Climate Dynamics and Dried-up Sea Bottom. *Ecosyst. Ecol. Dyn.* **2020**, *4*, 96–170. [CrossRef]
121. Adeniran, A.B.; Daniell, K.A. Transaqua: Power, Political Change and the Transnational Politics of a Water Megaproject. *Int. J. Water Resour. Dev.* **2021**, *37*, 234–255. [CrossRef]
122. Instanes, A.; Kokorev, V.; Janowicz, R.; Bruland, O.; Sand, K.; Prowse, T. Changes to Freshwater Systems Affecting Arctic Infrastructure and Natural Resources. *JGR Biogeosci.* **2016**, *121*, 567–585. [CrossRef]
123. Song, Y.; Zheng, H.; Chen, X.; Bao, A.; Lei, J.; Xu, W.; Luo, G.; Guan, Q. Desertification Extraction Based on a Microwave Backscattering Contribution Decomposition Model at the Dry Bottom of the Aral Sea. *Remote Sens.* **2021**, *13*, 4850. [CrossRef]
124. Simonova, Y.V.; Kasatkina, G.A.; Charykova, M.V.; Zhunusova, O.R. Soils of the Kuchuk-Kulunda Lakeside Landscapes (Altai Krai): Morphology, Salinization, Taxonomic Attribution. *POS* **2025**, *8*, e313. (In Russian) [CrossRef]
125. Romanov, A.N.; Bordonskiy, G.S.; Gurulev, A.A.; Khvostov, I.V.; Troshkin, D.N.; Peleneva, M.P.; Kazantsev, V.A.; Kozlov, A.K.; Orlov, A.O. On Some Features of Diurnal Dynamics of Solonchak Emissivity in Summer. *Int. J. Remote Sens.* **2025**, *46*, 1248–1256. [CrossRef]
126. Romanov, A.N.; Khvostov, I.V.; Ryabinin, I.V.; Romanov, D.A. Analysis of Hydrological Changes in Mineral Lakes in Northern Eurasia Based on SMOS Satellite Data. *Cosm. Res.* **2023**, *61*, S80–S88. [CrossRef]
127. Chen, Z.; Gao, X.; Lei, J. Dust Emission and Transport in the Aral Sea Region. *Geoderma* **2022**, *428*, 116177. [CrossRef]

128. Shevchenko, V.P.; Novigatskiy, A.N. Arctic branch of the global dust cycle. Modern issues in lithology and marine geology. In *Science. Training. Practice: Thesis of Reports/Scientific and Practical Forum Dedicated to the 270th Anniversary of the Lomonosov Moscow State University*; MAKS Press: Moscow, Russia, 2024; 258p. (In Russian)
129. Kulpin, E.S. The modern local socio-ecological crisis. *Hist. Mod.* **2007**, *1*, 146–158. (In Russian)
130. Sakiev, K.Z.; Zhumabekova, G.S.; Batyrbekova, L.S.; Ibraeva, A.D.; Khaidarov, K.K. Modern health problems of Aral Sea region. *Bull. Kazakh Natl. Med. Univ.* **2014**, *3*, 220–221. (In Russian)
131. Rozumbetov, K.U.; Najimov, I.I.; Nisanova, S.N.; Matchanov, A.T. Assessment of the health state of the population of the Aral Region. *Sci. Prog.* **2021**, *2*, 444–448. (In Russian)